Photoreceptor loss does not recruit neutrophils despite strong microglial activation

Derek Power,[1,2] Justin Elstrott,[3] Jesse Schallek[1,2,4]

Corresponding author: Jesse Schallek, Flaum Eye Institute, University of Rochester, Rochester, NY 14642, USA

Email: jschall3@ur.rochester.edu

Phone number: +1-585-273-4848

[1]Center for Visual Science, University of Rochester, Rochester, NY 14627, USA

[2]Flaum Eye Institute, University of Rochester, Rochester, NY 14642, USA

[3]Department of Translational Imaging, Genentech Inc., South San Francisco, CA 94080, USA

[4]Department of Neuroscience, University of Rochester, Rochester, NY 14642, USA

Impact statement: Systemic neutrophils do not respond to laser-induced photoreceptor damage despite the robust response from resident microglia

Financial support: Research was supported by the National Eye Institute of the National Institutes of Health under Award No. R01 EY028293, and P30 EY001319. Work was also supported by a collaborative grant from Genentech Inc, a Career Development Award and Career Advancement Award (Schallek) and Unrestricted Grant to the University of Rochester Department of Ophthalmology from Research to Prevent Blindness, New York, New York and the Dana Foundation David Mahoney Neuroimaging Award (Schallek)

Conflict of Interest statement: Portions of this work were funded by a collaborative grant from Genentech, Inc. (Elstrott) to examine the extent to which immune cells could be studied in the deep retina using adaptive optics. Schallek also has six patents held through the University of Rochester on adaptive optics technology.

Data availability statement: All data collected (~3 TB) is archived at the University of Rochester and is available upon request.

Abstract:

In response to central nervous system (CNS) injury, tissue resident immune cells such as microglia and circulating systemic neutrophils are often first responders. The degree to which these cells interact in response to CNS damage is poorly understood, and even less so, in the neural retina which poses a challenge for high resolution imaging in vivo. In this study, we deploy fluorescence adaptive optics scanning light ophthalmoscopy (AOSLO) to study fluorescent microglia and neutrophils in mice. We simultaneously track immune cell dynamics using label-free phase-contrast AOSLO at micron-level resolution. Retinal lesions were induced with 488 nm light focused onto photoreceptor (PR) outer segments. These lesions focally ablated PRs, with minimal collateral damage to cells above and below the plane of focus. We used in vivo (AOSLO, SLO and OCT) imaging to reveal the natural history of the microglial and neutrophil response from minutes-to-months after injury. While microglia showed dynamic and progressive immune response with cells migrating into the injury locus within 1-day after injury, neutrophils were not recruited despite close proximity to vessels carrying neutrophils only microns away. Post-mortem confocal microscopy confirmed in vivo findings. This work illustrates that microglial activation does not recruit neutrophils in response to acute, focal loss of photoreceptors, a condition encountered in many retinal diseases.

Introduction

In the mammalian retina, a rapid and coordinated immune response to infection or injury is important for maintaining tissue homeostasis. This is especially critical in the eye since mature retinal neurons do not typically regenerate, resulting in long-term functional losses for the host.[1,2] The retina is considered immune-

privileged and is equipped with a resident population of innate immune cells including microglia.[3,4] Under homeostatic conditions, microglia are distributed primarily in the inner retina, residing within nerve fiber layer (NFL), inner plexiform layer (IPL) and outer plexiform layers (OPL).[5,6], generally avoiding the nuclear layers of the retina. Microglia tile the retina and like their counterparts in the brain, exhibit long, thin cellular processes that continually probe the neuro-glial microenvironment.[4,7,8]

In addition to phagocytosing debris[9,10], regulating synaptic maintenance[11,12] and removing dead tissue[13,14], microglia can secrete chemokines to recruit other leukocytes to help fight infection and repair damaged tissue.[4,15–17] For a number of injuries, one of the first systemic responders recruited and activated by microglia are neutrophils.[18,19] Neutrophils comprise a large fraction of leukocytes in murine blood (7.4 – 33.9%, “young” C57BL/6J mice[20]). They assist in maintaining tissue homeostasis by neutralizing foreign agents, regulating the immune response, and processing dead tissue via phagocytosis[21,22]. Beyond these well-known functions, they are also implicated in becoming activated in conditions of shock and trauma[23]. Under inflammatory conditions, the spatiotemporal interplay between microglia and neutrophils is poorly understood. A missed window of interaction is highly problematic in histological study where a single time point only reveals a snapshot of the temporally complex immune response, which changes dynamically over time. Here, we use in vivo imaging to overcome these constraints.

Documenting interactions between immune cells in the retina over time has been challenged by insufficient resolution and contrast to visualize single immune cells in the living eye. Recently, advances in AOSLO imaging have provided micron-level resolution and enhanced contrast for imaging individual immune cells in the retina[7,24], and do so without requiring extrinsic dyes. This is achieved by using near infrared (NIR) light, to which the eye is less sensitive, and combining this with phase-contrast approaches[25–27]. In addition, AOSLO provides multi-modal information from confocal reflectance, phase-contrast and fluorescence modalities, which can reveal a variety of cell types simultaneously in the living eye. Here, we used confocal AOSLO (<6 μm axial resolution[28,29]) to track changes in reflectance at cellular scale. Phase-contrast AOSLO provides detail on vascular wall, single blood cells[30–32], PR somata[33], highly translucent retinal cells, and is particularly suited to image resident and systemic immune cells.[7,24] Simultaneous fluorescence imaging provides the ability to study fluorescently-labeled cells[26,29,34] and exogenous dyes[30,35] throughout the living retina. These modalities used in combination have recently provided detailed images of the retinal response to a model of human uveitis.[24,36] Together, these innovations now provide a platform to visualize, for the first time, the dynamic interplay between many immune cell types, each with a unique role in tissue inflammation. We combine these innovative modalities with conventional histology as well as commercial OCT to reveal the progressive nature of the cellular response to acute retinal injury.

As this work is in its early inception, we focus on one of many immune cell interactions, the interplay of two critical first responders to injury: neutrophils and microglia. To begin unraveling the complexities in this response, we examine the innate immune response to a deep retinal laser ablation model. Using AOSLO, we track and characterize the spatial, axial and temporal changes in microglia, neutrophils and retinal structure within hours, days and months after acute laser exposure.

Methods:

Key Resources Table				
Reagent type (species) or resource	**Designation**	**Source or reference**	**Identifiers**	**Additional information**
strain, strain background (*Mus musculus*)	C57BL/6J	The Jackson Laboratory	Strain #: 000664	
strain, strain background (*Mus musculus*)	CX3CR1-GFP	The Jackson Laboratory	Strain #: 005582	
strain, strain background (*Mus musculus*)	Catchup	Laboratory of M. Gunzer	C57BL/6-*Ly6g*(tm2621(CretdTomato) Arte	(Hasenberg *et al*. 2015) [37]
antibody	Ly-6G-647	Biolegend	Cat #: 127610 RRID:AB_1134159	IF (1:200)

other	DAPI stain	Cell Signaling Technology	Cat #: 4083	1:500 of 10 mg/ml stock
chemical compound, drug	Lipopolysac charide (LPS)	Sigma-Aldrich	Cat #: L4391	1 ng (1 µl) delivered intravitreally
software, algorithm	Cell counter plugin	Imagej FIJI	Cell counter plugin	Author: Kurt De Vos, Imagej version 1.53q

Mice

All experiments herein were approved by the University Committee on Animal Resources (protocol #: UCAR-2010-052E) and according to the Association for Research in Vision and Ophthalmology statement for the Use of Animals in Ophthalmic and Vision Research as well as institutional approvals by the University of Rochester. C57BL/6J (#000664, Jackson Labs, Bar Harbor, ME) mice were used to track the retinal phenotype after laser exposure. Heterozygous CX3CR1-GFP (#005582, Jackson Labs) mice were used to track GFP-expressing microglia. Mice with heterozygous transgenic expression of tdTomato in neutrophils ("Catchup" mice) were provided by the foundry lab of M. Gunzer.[37] 18 mice (10 male, 8 female) in total were used for *in vivo* imaging. 10

additional mice (5 male, 5 female) were used for *ex vivo* histology. Age for all mice used for this work were between post-natal weeks 6 - 24.

Preparation for *in vivo* imaging

Mice were anesthetized with intra-perotineal injection of ketamine (100 mg/kg) and xylazine (10 mg/kg). The pupil was dilated with 1% tropicamide (Sandoz, Basel, Switzerland) and 2.5% phenylephrine (Akorn, Lake Forest, IL). A custom contact lens (1.5 mm base curve, 3.2 mm diameter, +10 diopter power, Advanced Vision Technologies, Lakewood, CO) was fitted to the eye. For a subset of experiments, 50 mg/kg fluorescein (AK-FLUOR, Akorn, Decatur, IL) was administered by intra-perotineal injection to confirm vascular integrity and perfusion status after injury. During AOSLO imaging, anesthesia was supplemented with 1% (v/v) isoflurane in oxygen and mice were maintained at 37°C via electric heat pad. Eye hydration was maintained throughout imaging with regular application of saline eye drops (Refresh tears, Allergan, Sydney, Australia) and lubricating eye gel (Genteal, Alcon Laboratories Inc. Fort Worth, TX) in combination with rigid contact lens described above. Mice were placed in a positioning frame with 6-degrees of freedom to allow for stable animal positioning and to aid in retinal navigation relative to the beam of the AOSLO and OCT.

***In vivo* AOSLO imaging**

Four light sources were used for AOSLO imaging. A 904 nm diode source (12 μW, Qphotonics, Ann Harbor, MI) was used for wavefront sensing. A second 796 nm superluminescent diode (196 μW, Superlum, Cork, Ireland) was used for reflectance imaging, including confocal and phase contrast modes.[29,30] A third 488 nm light source (56 μW, Toptica Photonics, Farmington, NY) was used to visualize GFP-positive microglia in CX3CR1-GFP mice. A fourth 561 nm light source (95 μW, Toptica Photonics) was used to visualize tdTomato-positive neutrophils in Catchup mice. All light sources were fiber-coupled and were axially combined through the AOSLO system in a free-space design[29]. Fast (15.4 kHz) and slow (25 Hz) scanners create a raster scan pattern, which is relayed through a series of afocal telescopes to and from the eye. A Shack-Hartmann wavefront sensor (consisting of a lenslet array and a Rolera XR camera, QImaging, Surrey, Canada) measures the aberrations of the eye and a 97 actuator deformable mirror (ALPAO, Montbonnot-Saint-Martin, France) provided the wavefront correction. Reflected 796 nm light was collected with a photomultiplier tube (H7422-50, Hamamatsu Photonics, Hamamatsu, Japan). All confocal reflectance images were captured with a 30 μm pinhole (1.3 Airy Disc Diameters, ADD). Phase-contrast was achieved by displacing the pinhole relative to the principal axis of the detection plane as previously described.[26] Fluorescence was captured with a photomultiplier tube (H7422-40, Hamamatsu) either coupled with a 520Δ35 band-pass filter (FF01-520/35-25, Semrock, Rochester, NY) for GFP emission, or a 630Δ92 band-pass filter (FF01-630/92-25, Semrock) for tdTomato

emission. All fluorescent images were captured with a confocal 50 μm pinhole (2.1 ADD). Image field sizes were either 4.98° x 3.95° or 2.39° x 1.94°. NIR and visible imaging channels were made coplanar, compensating for longitudinal chromatic aberration by independently focusing each light source so it projected onto the same axial structure in the retina. Through-focus acquisitions were acquired by sequentially changing the focus from nerve fiber layer through to the PR outer segments by using the defocus term on the custom adaptive optics control software. This strategy allowed depth imaging while keeping all visible and NIR sources conjugate to the same axial plane.

As described previously, red blood cell (RBC) imaging was achieved by combining phase-contrast imaging with a strategy to arrest the slow galvanometer scanner and let the resonant scanner project a single “line” on the retina. This enabled RBC flux imaging by positioning this line orthogonal to the direction of flow for single capillaries. As blood cells moved through capillaries, they were “self-scanned” producing images of RBCs in space/time images[30] (Figure 4 – figure supplement 1b + f). Scan angle for this modality was 0.71°.

PR laser damage model and post-injury time points for imaging

488 nm light (Continuous wave Laser diode, ±4 nm bandwidth, Toptica Photonics) was used to create an acute laser injury. Laser light was projected through the AOSLO and focused onto the PR outer segments. To create damage, 785 μW of 488 nm light was focused onto the PR outer segments for 3 minutes in a single line on the retina subtending 24 x 1 μm to concentrate the

power to a small focal region. Laser injuries were placed between 5-15° from the optic disc. To avoid absorption confounds, we avoided placing lesions beneath large retinal vessels. For experiments examining neutrophil involvement, lesions were placed less than ~100 microns away from retinal veins and within microns of capillaries to increase the chance of extravasation through these preferred pathways in the retina[38–40]. As many as four such lesions were placed per retina (Figure 1). We chose to use the above protocol as an established way to create modest, consistent and reproducible outer retinal damage.

Throughout this work, we assessed the effects of the laser injury for the following time points: baseline/control, 1 day (defined as 18 – 28 hours post-damage), 3 days, 7 days and 2 months.

In vivo **SLO, and OCT imaging**

To confirm global ocular health and changes imparted by the laser damage, a commercial Heidelberg Spectralis system (Heidelberg, Germany) was used to acquire scanning laser ophthalmoscopy (SLO) and optical coherence tomography (OCT) images. 30° and 55° fields were used for SLO acquisitions. The 30° field was used for OCT acquisitions. The wider imaging fields allowed for global views not only of damage locations, but also adjacent, non-damaged retina. For some experiments, fluorescein angiography was captured by imaging the retina within 10 minutes of fluorescein administration (details above). As an

additional advantage, the fluorescence mode of the Spectralis enabled wide-field images of GFP positive microglia (Figure 5a, right).

OCT was acquired with the following settings: ART 16 (automatic real-time tracking) was used to average B-scans to improve signal. To capture several damage locations in a single field, we used a coarse scan area (61 B-scans over a 1.02 x 0.85 mm window, Figure 1c). A dense 3D data cube was also captured (513 x 171 µm, 49 progressive B-scans, Figure 2a) to provide the most detailed information regarding the axial nature of the laser damage. “Follow-up” mode, which allows HRA software to return to the same retinal location, was used whenever possible. To reveal the cross-sectional profile for each lesion, several adjacent B-scans were spatially averaged (~30 µm).

Preparation for *ex vivo* imaging

Mice were euthanized by CO_2 asphyxiation followed by rapid cervical dislocation. Eyes were enucleated and placed in 4% paraformaldehyde (PFA, diluted from: #15714-S, Electron Microscopy Sciences, Hatfield, Pennsylvania) in 1x phosphate buffered saline (PBS, #806552, Sigma-Aldrich, St. Louis, MO) within 5 minutes of asphyxiation. Intact eye globes were left in PFA fix for one hour at room temperature. Eyes were dissected to remove the cornea, lens and vitreous. Each eye cup was placed in one well of a 24-well plate containing 0.5 ml of 0.8% PFA and left overnight at 4°C. The retina was separated from the retinal pigmented epithelium/choroid with attention to preserve inner retinal layers “up”

orientation. If not applying antibody, the tissue was directly flat mounted (see below). For antibody staining, the retina was placed in 1x BD perm/wash buffer (#554723, BD Biosciences, Franklin Lakes, NJ) with 5% donkey serum (#D9663, Sigma-Aldrich) diluted in PBS for overnight incubation at room temperature with gentle shaking. The following was performed in the dark. Ly-6G-647 antibody (1:200, #127610, RRID:AB_1134159, BioLegend, San Diego, CA) and DAPI (1:500 of 10 mg/ml stock, #4083, Cell Signaling Technology, Danvers, MA) were diluted in 1x perm/wash buffer and retinas were incubated for 3 days at room temperature with gentle shaking. Retinas were washed with PBS three times over three hours. The retina was cut into 4 radially symmetrical petals, flat-mounted on a glass slide in ~40 µl of Vectashield mounting buffer (H-1000-10, Vector labs, Newark, CA) with a #1.5 cover slip (#260406, Ted Pella Inc., Redding, CA), sealed with nail polish and stored at 4°C until imaged.

Endotoxin-Induced Uveitis protocol

To serve as a positive control and show evidence of known neutrophil invasion, we adopted the endotoxin-induced uveitis model to confirm that fluorescent neutrophils could be observed in vivo with AOSLO. This was performed in two mice. The endotoxin-induced uveitis model has been described previously.[36,41] Briefly, we performed intravitreal injections of lipopolysaccharide (LPS, #L4391, Sigma-Aldrich). Mice were anesthetized with ketamine and xylazine. A 34 gauge Hamilton needle was used to deliver 1 µL (1 ng) of LPS diluted in PBS into the vitreous space posterior to the limbus. 1 day post-LPS injection, mice were either

imaged with AOSLO (Catchup mice) or collected for *ex vivo* histology (Ly-6G-647 stained C57BL/6J mice) to confirm fluorescent neutrophil presence in the neural parenchyma.

***Ex vivo* confocal imaging**

Whole-mount retinas were imaged with a Nikon A1 confocal microscope (Melville, NY). DAPI (405 nm ex, 441Δ66 nm em), CX3CR1-GFP (488 nm ex, 525Δ50 nm em), and Catchup/anti-Ly-6G-647 (635 nm ex, 665Δ50 nm em) were simultaneously imaged. Z-stacks at control or laser-damaged locations were acquired with a 60x oil objective, producing images that were 295 x 295 µm. Z-stack axial sectioning was performed with either 0.1 or 0.5 µm step size. Larger (796 x 796 µm) 60x z-stacks were acquired by blending several 60x z-stack acquisitions (3x3, 15% overlap) using the native Nikon NIS Elements software.

AOSLO image processing

To correct for residual motion from heart rate and respiration, AOSLO images were registered with a custom cross-correlation-based frame registration software.[42,43] Motion correction was also applied to simultaneously collected fluorescence images. After registration, confocal, phase-contrast and fluorescence AOSLO images were temporally averaged (250 frames, 10 seconds). Blood perfusion maps were computed by calculating the standard deviation of pixel intensity over 30 seconds[34] (Figure 4).

***Ex vivo* confocal image processing**

Imagej FIJI (free NIH software)[44] was used to view and manage data files. Confocal z-stacks were re-sliced (X-Z dimension) to visualize fluorescence depth profiles.

INL + ONL nuclei quantification

Raw DAPI z-stacks were used for manual counting of nuclei (n = 10 mice, 3 unique regions per time point). Analysis regions were circular, with a 50 µm diameter (roughly corresponding to the size and shape of the damage region seen with confocal AOSLO, Figure 3e) and analyzed in depth producing volumetric cylinders through the INL or outer nuclear layer (ONL, Figure 3d). Nuclei were counted manually using the “Cell Counter” plugin in Imagej (Author: Kurt De Vos, Imagej version 1.53q).

PR + Microglia nuclei volume quantification

A single DAPI-stained z-stack (OPL + ONL) from a CX3CR1-GFP mouse was used to quantify nuclear volume of PR’s (n = 20) and microglia (n = 14). Data was centered at a lesion location 3 days post-laser exposure. Imagej was used to manually measure the en-face diameter of nuclei in their short and long axis. We averaged the two measurements and assumed spherical shape for analysis. These measurements aided in the differentiation of PR’s, invading microglia and PR phagosomes.

Quantification of RBC flux in capillaries

Using the line-scan approach across single capillaries[30,45,46], we quantified RBC flux within an epoch of 1 second. This spanned several cardiac cycles.[32,47] To improve SNR, space-time images were convolved with a Gaussian spatio-temporal filter (σ = 7.5 pixels, 0.33 μm). This strategy did not interfere with spatial resolution as pixels oversample the optical point-spread of the AOSLO by >20x.[30] RBC flux was determined by manually marking blood cells using the "Cell counter" plugin in Imagej.

Neutrophil density quantification

Ly-6G-647-stained retinal tissue was used to manually count neutrophils within montaged 796 x 796 μm z-stacks. Cells were counted at control (n = 4 locations, 2 mice) and lesioned (n = 4 locations, 2 mice) locations using the "Cell Counter" Imagej plugin. All values are reported as mean ± SD. There were no data points omitted from any of the analysis reported in this work.

Results:

Characterization of deep focal laser damage

Four complementary imaging modalities were used to evaluate the nature and localization of the focal laser damage induced by 488 nm light: wide field SLO, OCT, AOSLO and post-mortem histology. Each is reported in turn below.

Laser damage induces focal hyperreflective lesions in outer retina imaged with wide-field SLO

To observe global and focal retinal health, we used commercial SLO. 1 day post-488 nm light exposure, both NIR and blue reflectance modalities showed hyperreflective lesions, most apparent at a deeper retinal focus position. When SLO focus was brought to the inner retina, lesions were not visible and retina appeared otherwise healthy (Figure 1b). Despite the deep retinal damage phenotype, fluorescein angiography did not reveal dye leakage (Figure 1b, bottom), indicating the blood retinal barrier remained intact.

OCT B-scans reveal outer retinal hyperreflection without inner retinal damage

To assist in determination of which retinal layers are damaged by the 488 nm laser, we used OCT. Within 30 minutes post-laser exposure, OCT revealed a zone of hyperreflection within the ONL (Figure 2 – figure supplement 1). 1 day post-lesion, the focal hyperreflection remained localized to the ONL (~50 microns wide, Figure 1c, 2a). With OCT, the retina laterally adjacent to damage foci appeared normal. The hyperreflective phenotype persisted through 7 days post-damage and was cleared by 2 months (Figure 2a). There did not appear to be any cellular excavation, “cratering” or evidence of edema for any post-exposure time point assessed. Despite the axially localized hyperreflective phenotype, Bruch’s membrane appeared intact for all time points assessed. This was evidenced by lack of fluorescein leakage at the site of lesion. Additionally, retinal vessels appeared normal in OCT B-scans aligning with findings from fluorescein angiography, vascular perfusion and histology (discussed below).

AOSLO reveals outer retinal damage with confocal and phase-contrast modalities

Confocal AOSLO provided micron-level detail of the lesioned area. Confirming OCT findings, we observed hyperreflective changes localized within the ONL that were, by 1 day, the brightest at the OPL/ONL interface, shown in Figure 2b. The AOSLO has an axial resolution near 6 μm[29] and thus evidence of retinal capillaries at the deepest vascular stratification acted as an axial landmark for the OPL. At this plane, the lesions manifest as an elliptical region with the long axis in the direction of the linescan used to create the lesion. Tracking this region over time, showed most prominent hyperreflectivity at 1 day post lesion, with diminishing size and brightness by day 3 and 7. The hyperreflective phenotype was largely diminished by 2 months post-exposure (Figure 2b).

Using phase-contrast AOSLO also allowed visualization of translucent cells within the retina which enabled us to image PR somas of the ONL[26,33]. Normally, the ONL is comprised of 8-12 PR somata that are axially stacked[33,48]. We found that the dense packing of individual somata was disrupted 1 day post-exposure (~50 μm ovoid, Figure 2c), suggesting degradation or ablation of the cell membrane.

Confirmation of outer retinal cell loss using post-mortem histology

To assess the extent of cell loss caused by focal laser exposure, we performed DAPI staining on whole-mount retinal tissue using the same time points

assessed previously for *in vivo* imaging. 1 day after laser exposure, we observed mild thickening of the ONL compared to unexposed locations only microns away. At 3 and 7 days, local ONL thinning was observed (Figure 3a). En-face planes at multiple layers within the ONL revealed a loss of PR nuclei in the outer aspect of the ONL for 3 and 7 day time points (Figure 3c). The inner ONL exhibited little evidence of cell loss (Figure 3b), illustrating the precise axial confinement of the laser damage being induced by this method. By 2 months, the lesion's overall appearance and ONL thickness returned to baseline (Figure 3a-c). This histological finding corroborates the OCT findings observed *in vivo*.

ONL nuclear counts were reduced at locations of laser exposure. In comparison to control locations (501317 nuclei/mm^2 ± 46198 nuclei/mm^2, mean ±SD, similar to previous work[49]), at 3 and 7 days post-exposure, we found a corresponding reduction in the density of ONL nuclei of 18% (408965 nuclei/mm^2 ± 25621 nuclei/mm^2) and 27% (367542 nuclei/mm^2 ± 9038 nuclei/mm^2) respectively. Calculated in comparison to control locations, the 3 and 7 day data resulted in p-values of 0.17 and 0.07, respectively (Student's, paired two-tailed, t-test). 2 months after damage, PR nuclear densities were indistinguishable from that of control (Figure 3f, gray bars). Despite losses of PR nuclei, total cell nuclei within the INL remained unchanged for all time points (Figure 3f, black bars). These data indicate that the laser exposure focally ablated PR's whilst leaving inner retinal cells intact.

Retinal vasculature unaffected by deep retinal lesion

A concern with laser lesions of this type is that it may coagulate large vessels or capillaries. Motion contrast[27,30] images revealed that the vasculature remained perfused from hours to months after laser damage suggesting that acute or long term changes are not imparted by the laser injury (Figure 4). None of the primary vascular stratifications within the NFL, IPL and OPL of the mouse retina[34] showed stopped flow as a result of the laser lesion, reinforcing the findings above regarding the axial confinement of the damage to the outer retina.

In addition to perfusion status, phase-contrast AOSLO also permitted analysis of single blood cell flux within capillaries[30,50]. We tracked capillary flux at different retinal depths within and above damage sites (IPL, OPL, 1 capillary each, Figure 4 – figure supplement 1a). Blood cell flux for capillaries within lesion locations were within the range of normal flux for the C57BL/6J mouse[50] (Figure 4 – figure supplement 2b, c). Flux tracked from hours to days in these capillaries changed synchronously, displaying positive linear correlation (R^2 = 0.59, Figure 4 – figure supplement 1c, d). This suggested any such changes in flux were a property of systemic perfusion, rather than locally imparted changes in flow due to the lesion. As an additional control, we evaluated blood flux in two distant capillaries; one located 10-15° temporal of the optic disc (lesion location) and another of equivalent eccentricity on the nasal side (control, Figure 4 – figure supplement 1e). Both capillaries displayed similar flux values from minutes to 2 months post-injury (Figure 4 – figure supplement 1f, g) resulting in positive linear correlation (R^2 = 0.78, Figure 4 – figure supplement 1h). Taken together, these

findings suggest lesions do not rupture or stall blood flow in capillaries, nor do they appreciably impact total RBC delivery in the capillary network.

PR laser injury promotes a robust response in nearby microglia

To observe the microglial response to PR laser injury, we imaged fluorescent microglia in CX3CR1-GFP mice with both SLO and AOSLO. 1 day after injury, SLO revealed bright, focal congregations of microglia at injury locations. This was in contrast to undamaged locations which maintained a distribution resembling lateral tiling (Figure 5a, b). The global visualization of microglia was augmented by high resolution fluorescence AOSLO, providing enhanced detail of the microglial response to laser injury, especially cellular process detail[7,51]. Whereas AOSLO imaging of microglia in the healthy retina displayed a distributed array of microglia with ramified processes (Figure 5c, left), laser damaged locations showed a congregation of cells 1 day post-injury with less lateral ramification (Figure 5c, right). Within hours of the laser exposure, we did not observe a photo-bleaching or death of regional microglia suggesting that while the laser exposure was sufficient to damage PR's, it left inner retinal microglia intact.

A standing question in OCT/confocal AOSLO interpretation is whether microglia contribute or directly produce the hyperreflective phenotype seen in axial B-scans and en-face fundus images[52,53]. With confocal AOSLO, we find that the hyperreflective phenotype is visible as early as 30 minutes and becomes

slightly larger and brighter by 90 minutes. During these time points, simultaneously imaged microglia remained ramified and maintained a tiled arrangement, indicating that microglial are not the initial source of the lesion-induced hyperreflective appearance (Figure 6 – figure supplement 1).

We returned to the same laser-damaged locations to capture microglial appearance at baseline, 1, 3, 7 day and 2 month time points with AOSLO to track the natural history of the microglial response to PR damage. At 1 day post-injury, damage locations displayed aggregations of microglia. The surrounding microglia displayed process polarization with extensions projecting toward the injury (Figure 6). By days 3 and 7, microglia exhibited fewer lateral projections and somas have migrated into the ONL where they do not normally reside (Figure 6). By 2 months post-injury, the hyperreflective phenotype was absent and microglia once again occupied only the inner retina. The axial and lateral microglial distribution at 2 months after lesion was similar to baseline (Figure 6). Additionally, cell morphology once again showed radially symmetrical branching projections, similar to those prior to laser injury.

With phase-contrast imaging targeting the ONL, we documented a rare event of putative pseudopod extension at a lesion site (Figure 5 – video 1). Given the axial complexity of microglia in this layer (Figure 9 – figure supplement 2c) it is now possible that microglial process dynamics may be revealed with this label-free approach.

Despite robust microglial involvement, neutrophils do not extravasate

While we observed a robust microglial response to PR damage, there was no evidence of neutrophil involvement at the times we examined (1, 3, 7 day, and 2 month follow-up).

In vivo fluorescence imaging allowed us to track neutrophils with AOSLO in “Catchup” mice[37]. In healthy mice, we observed a sparse population of circulating neutrophils flowing quickly within the largest retinal vessels (Figure 7 – video 1). We also observed neutrophils moving through single capillary branches (Figure 7 – video 2). This provided evidence that neutrophils could be directly observed in vivo, where they are moving at exceptionally fast speed[32]. Within capillaries, we found that neutrophils show deformation within the small confines of the capillary lumen, often resulting in tube or pill-shaped neutrophil morphology seen both in vivo and ex vivo (Figure 7b, top).

After inducing laser lesion, we found no evidence of neutrophil aggregation or extravasation for any time point assessed (Figure 8). There was also a notable lack of rolling/crawling neutrophils (or any putative leukocyte) in large arterioles or venules surrounding the injury (Figure 8 – video 1). The deepest retinal neutrophils, closest to the ONL lesion, were occasionally detected within the deepest retinal capillaries. However, these neutrophils stayed within the retinal vasculature, as evidenced by their pill-shaped morphology and passage routes that follow the known vascular paths seen in confocal/phase

contrast imaging (Figure 8 – video 2). Just like healthy mice, leukocytes, including neutrophils often impede flow due to their large size (13.7 µm[54]) as they must compress through capillaries <7 µm in diameter[50]. However, we found no evidence of permanently stopped flow, as the rare stalls would re-perfuse similar to those previously characterized in healthy mice (Figure 7a).[50]

As a positive control, we used the endotoxin-induced uveitis model in Catchup mice to show evidence that we could image extravasated neutrophils. This model is known to induce a strong neutrophil response. With fluorescence AOSLO, we found aggregation of Catchup-positive neutrophils within the retinal parenchyma, providing confirmation that extravasated neutrophils can be imaged with this modality. Moreover, we found that neutrophils that have extravasated into the retinal parenchyma tended to have a more spherical morphology rather than the compressed, pill-shaped morphology of neutrophils within capillaries (Video 2).

***Ex vivo* analysis confirms *in vivo* findings**

To confirm our *in vivo* findings and make certain that no neutrophils evaded detection with *in vivo* imaging, we examined fluorescent microglia and neutrophils in laser-damaged retinal whole-mounts imaged with confocal microscopy. Both the spatial and progressive nature of the microglial response to PR damage corroborated *in vivo* findings (Figure 6 vs Figure 9 – figure supplement 1). Similarly, we found a general lack of neutrophil response.

Ex vivo: Microglia display dynamic changes in morphology in lesion areas

Without laser damage, microglia exhibited a tiled distribution and stellate morphology with highly-ramified branching patterns (Figure 9a). 1 day after laser exposure, microglial somas aggregated to the lesion location. They began to migrate into the ONL and the most notable phenotype was a change from the ramified, and pancake-flat morphology seen in the healthy retina, to a dagger-like axial morphology. (Figure 9a + Video 1). At 3 and 7 days after lesion, microglia migrated deeper into the outer retina and remained aggregated with an axially elongated phenotype. 2 months after laser lesion, microglial somas were no longer found in the ONL. Instead, microglia redistributed similar to that of the healthy retina (Figure 9a), once again co-stratifying predominantly with the NFL and plexiform layers of the retina.

Whereas we found a robust response of deep microglia at the OPL to PR injury, we observed little migratory response of the microglia in the NFL or IPL (Figure 9 + Figure 9 – figure supplement 1) suggesting axial and lateral constraints on the extent of microglial recruitment.

Microglia form PR-containing phagosomes

A detailed examination of the microglial involvement with PR somata in response to PR injury revealed unique microglia-PR interactions within the ONL. In cross-section, PR cells comprise a large portion of the retina reaching from the outer-segment tip, inner segments, somata and spherule/pedicle synaptic contacts at

the OPL. Likewise, we saw microglial involvement with all of these layers. Within 1 day, we found microglial processes interspersed within the dense aggregation of PR somata within the ONL. Amoeboid cells enveloped the somata of PR's and phagocytosis was detected 1, 3 and 7 days post-laser exposure (Figure 9 – figure supplement 2). Confocal microscopy revealed GFP-positive processes surrounding PR nuclei, engulfing multiple somata (Figure 9 – figure supplement 2a, c). By 3 days, microglial processes and somas were found to migrate deeper, now with processes extending into the distal portions of the PR cells including the inner/outer segments. By two months microglial processes and somas had retreated out of the ONL.

The DAPI nuclear stain combined with confocal microscopy not only helped us discern retinal neurons, but also allowed us to differentiate between microglia and phagocytosed PR's. Two features were different from PR and microglial nuclei. First, whereas PR's displayed a uniform, homogeneous nuclear fluorescence, microglial nuclei showed a mottled, and heterogenous DAPI appearance (Figure 9 - figure supplement 2a). Second, microglia nuclei were nearly 3x larger in volume compared to healthy and damaged PR nuclei. Microglia had nuclear volume of 110 ± 42 μm^3 and PR nuclei were 35 ± 5 μm^3 ($p < 0.001$, Figure 9 – figure supplement 2b). PR nuclei within microglial phagosomes displayed similar nuclear volume compared to adjacent PR's in undamaged locations (Figure 9 – figure supplement 2a).

***Ex vivo*: At lesion sites, neutrophils remain within the retinal vasculature**

Corroborating in vivo AOSLO findings we did not find neutrophil aggregation or extravasation in response to laser damage at any of the time points examined. *Ex vivo* microscopy revealed that neutrophils were found within the vascular network and did not extravasate into the neural retina. Very few neutrophils were found in lesioned retinas, comparable to the paucity of neutrophils found in healthy retinas. The few detected neutrophils were remnants of those found within the capillary network at point of death. Detailed Z-stacks at 60x magnification revealed "pill-shaped" morphology similar to that seen *in vivo*, where neutrophils are compressed within capillaries. In one exceptional example (1 day post-damage, Figure 9c,d), we observed two neutrophils in a single z-stack, one in a capillary (1) and one at a capillary branch point (2), but none were observed to have left the confines of the vasculature suggesting they were not recruited by activated microglia.

Retinal neutrophil concentrations were quantified from larger z-stacks (796 x 796 μm, Figure 10a). Control locations (n = 2 mice, 4 z-stacks) had 15 ± 8 neutrophils per mm^2 of retina whereas lesioned locations (n = 2 mice, 4 z-stacks) had 23 ± 5 neutrophils per mm^2 of retina (Figure 10b). The difference between control and lesioned groups were not statistically significant ($p = 0.19$).

Finally, when we rendered confocal Z-stacks in cross-sectional view, we discovered that the few fluorescent neutrophils present were found colocalized within the tri-layered vascular stratifications of the mouse retina [34,55,56]. None were found in non-vascular layers (Figure 9). Taken together, all *ex vivo* data

indicates that neutrophils remain localized within vessels, suggesting that neutrophils do not extravasate or aggregate in response to this laser lesion model, regardless of the robust phagocytic microglial response. These data corroborate the in vivo findings.

Discussion:

Summary

In many retinal diseases, resident microglial populations are found to exhibit cross-talk with systemic immune cells[15,18]. The complex temporal dynamics between resident and systemic immune cells unfolds from seconds-to-months and has been poorly characterized due to lack of resolution, sufficient contrast and a non-destructive imaging approach that can track changes over time. Here, our engineering advance overcomes these limitations by using phase-contrast and fluorescent imaging with adaptive optics to visualize the interaction of multiple cell types. With this advanced imaging technology, we reveal the absence of neutrophil involvement in response to an acute injury, despite progressive changes in microglial activity and morphology. Here we discuss the implications of such findings in the context of retinal damage and more broadly, to retinal disease.

Focal retinal lesions for tracking the immune response

Light damage offers a number of advantages for creating acute damage in the retina. It offers placement precision that is better controlled than other acute and

invasive methods, such as incision/poke injuries[57], retinal detachment[58] and chemical injury[59,60]. In the mouse, focal light dosage comes with greater axial confinement within the retina by nature of the high numerical aperture of the mouse eye[29] which imposes minimal collateral damage to layers above or below the plane of focus (Figure 1a). The laser exposure protocol employed here was highly reproducible as ~95% of light exposures resulted in retinal damage of similar size and hyperreflective phenotype.

Seminal studies in the brain have used focal light exposure to induce acute microglial response to targeted areas.[61,62] Since then, it has been a popular damage model. Focal lesions in the retina have been conducted in a number of popular animal models including mouse[63,64], macaque[65–67] and cats.[68,69] Laser damage is also clinically relevant as it is both experienced with accidental laser exposure[70,71] as well as purposeful ablation used in photocoagulation and as a therapy for retinal ischemic disease, retinopathy of prematurity[72] and diabetic retinopathy[73]. Thus our results shed light toward the immune response that may be imparted due to phototoxic damage. More widely however, this approach may be considered when investigating how native microglia may signal to the systemic immune system in response to any acute injury or chronic photoreceptor loss in aging/diseased retinas.

Titration of the 488 nm laser leads to mild retinal damage

While it is beyond the scope of this report to catalog the vast parameter space in which light may impose damage in the retina, it is noteworthy to discuss that the exposure intensity, subtended angle and duration of the CW light source we used delivered an intentionally mild damage to the retina. Using dosages too high would run the risk of collateral damage to the blood retinal barrier or Bruch's membrane[74] which could cause a choroidal neovascularization phenotype[75]. Either of these would be undesirable for studying the native/systemic immune response as it would potentially confound the traditional extravasation pathways of the inflammatory system[24,76]. Instead, we chose our laser exposure condition to impart a weak, but reproducible loss in photoreceptors while minimizing collateral damage to the cells above and below the plane of focus.

With OCT, we see the primary damage phenotype localized to the OPL/ONL bands (Figures 1, 2) with visibly undetectable change in the anatomy of the inner retina. Histology corroborated this finding since the only layer showing quantifiable cell loss was the photoreceptor layer (Figure 3).

Progressive PR loss and morphology of the lesion tracked over time

The amount of light we delivered did not immediately ablate photoreceptors as the peak cell loss wasn't observed until 3-7 days after laser exposure suggesting a progressive damage phenotype of apoptosis or necroptotic death rather than direct ablation. Histology showed a ~27% reduction in PR nuclei 7 days post lesion. The total number of PR nuclei within the lesion location returned to values

similar to baseline by 2 months, which was surprising given that PRs do not regenerate. Our interpretation is that adjacent PRs spill into the region of loss, similar to what several have described previously[65,77]. Corroborating the histological finding of mild cell loss, is the in vivo OCT data which shows no evidence of local edema, cavitation or excavation of the ONL after PR loss (Figure 2a). The return of the appearance, thickness and redistribution of cells within the ablated location indicates that retinal remodeling occurs within a 2 month window. The concurrence of microglia in these outer retinal bands (where they are normally absent in health[78]) support the hypothesis that microglia localized to this region to facilitate a phagocytic injury response and perhaps contribute toward synaptic remodeling[11].

The hyperreflective phenotype does not arise from microglia or neutrophils

Light damage is known to create a hyper-reflective bands in OCT imaging [66,79,80]. A common speculation is that the increased backscatter may arise from the local inflammatory cells that activate or move into the damage location. In our data, confocal AOSLO and OCT revealed a hyperreflective band at the OPL and ONL after 488 nm light exposure (Figure 2a, b). However, we found that the hyperreflective bands appeared within 30 minutes after the laser injury. This phenotype preceded any detectable microglial migration toward the damage location (Figure 2 – figure supplement 1 and Figure 6 – figure supplement 1). We thus conclude that the in vivo hyperreflective phenotype is not caused by microglial cell activity or aggregation.

Direct activation of microglia from 488 nm light exposure was minimal

It is conceivable that 488 nm light used for either imaging (56 μW) or imparting damage (785 μW) might activate the GFP-containing microglia in the Cx3CR1 mouse model used here. However, several lines of evidence speak against this possibility. 1) We did not observe photobleaching of CX3CR1 positive cells in response to the damage suggesting the fluorescence imaging light was insufficient to damage microglia. 2) The focal plane was adjusted using the optics of the AOSLO, focusing the light such that the dose was most axially concentrated onto the outer retina when performing retinal injury. Thus, the light dosage received by the microglia above was defocused and less than the targeted PR layer (Figure 1a). 3) Histology showed no evident necrotic/apoptotic microglial morphologies and were similar to cells at undamaged locations.

488 nm laser lesion does not photocoagulate or alter retinal circulation

Despite imparting damage to the photoreceptors, the damage regime used here did not alter the perfusion of the retinal circulation. We show three independent measures that blood flow is uninterrupted, despite quantifiable PR loss and activation of microglia. 1) Fluorescein angiography (Figure 1b, bottom) displays intact vasculature passing through and above lesion locations. The absence of fluorescein leakage indicates that the lesion did not compromise the blood-retinal barrier. Additionally, there was no indication of a perforated Bruch's membrane. 2) AOSLO motion contrast vascular maps [25,30,34] displayed persistent blood

perfusion inside vessels near laser lesion sites (Figure 4). This indicated that single cell perfusion through the capillaries above and adjacent to the regional damage was maintained 3) Capillary line scans indicate that RBC flux was not modified at lesion locations and fell within the normal range[30,50] (Figure 4 – figure supplement 1). Altogether, these three lines of evidence indicate that the 488 nm light exposure does not impart perfusion changes within the retinal vasculature.

Microglial/neutrophil discrimination using label-free phase contrast

In this work, we use fluorescence to validate the presence and dynamics of microglia and neutrophils in response to PR damage. We have found that microglia and neutrophils show a number of differences that may be useful for identifying their type without the need for fluorescent labels. For example: under healthy conditions, these cells exhibit morphological differences: retinal microglia exhibit processes that emanate from the soma, exhibiting an arbor that actively surveys a large patch of retina, while neutrophils are spheroid, sometimes presenting as cylinders when squeezing through retinal capillaries. Another difference lies in their motility: neutrophils remain within the vasculature, often times traveling at high speeds while microglial somas generally remain stationary as they monitor the local microenvironment. With a strong base-of-knowledge about the morphological and behavioral features to expect for each cell type, label-free imaging could discriminate not just immune cells, but other retinal cells as well in the future.[24] This is particularly promising when considering translating

these observations into the human population where dyes and fluorescent agents are used sparingly.

Resident microglia do not need systemic neutrophils for resolution of mild laser-damage

The CNS and retina, unlike other peripheral tissues, cannot suffer from excess inflammation as there may be dire functional consequences. Therefore it is possible that microglia protect against exorbitant inflammation by modulating the recruitment of systemic inflammatory cells.[4,15–17] Of these, neutrophils are often one of the first systemic responders. Despite their helpful roles in other tissues, neutrophils can secrete neurotoxic compounds that could present a danger to the CNS.[81] Given their conflicted role in the body, we ask the question: to what extent do neutrophils respond to acute neural loss in the retina? Retinal cells are lost with age[82] and disease[83] and yet, for the organism, visual perception must persist. In this laser lesion model, we ablate 27% of the photoreceptors in a 50 µm region. This acute damage model can begin to provide clues about how the immune system responds when photoreceptors are lost in disease.

We find that microglia undergo a rapid and progressive response to this injury. We show evidence of PR phagocytosis (Figure 9 - figure supplement 2), interaction with neighboring microglia (Figure 9 – figure supplement 1) and they are also axially positioned to facilitate retinal remodeling (Figure 9). Furthermore, throughout the temporal evolution of the microglial response, we find no evidence

of neutrophil recruitment despite the damage being within 10s of microns from retinal vessels that carry systemic neutrophils. At the onset of the neutrophil extravasation cascade, endothelial cells in the vicinity of inflamed tissue typically elevate the expression of adhesion molecules, facilitating the adherence and extravasation of circulating neutrophils.[84] Furthermore, neutrophils are dependent on priming events as prerequisite to further activation and engagement of their effector functions.[85,86] Based on our data, we suggest that although microglia show a strong and lasting activation, at no time point from seconds-to-months, are the damage-associated molecular patterns or chemotactic gradients strong enough to recruit neutrophils in response to this damage. This is evidenced in our data from two key observations: 1) in response to laser injury, we saw no examples of systemic leukocytes rolling in vessels adjacent to injury locations (Figure 8 – video 1). 2) Using fluorescence, we did not observe adherent or extravasated neutrophils adjacent to imparted photoreceptor loss (Figure 8). This may suggest that the region of insult is too small, or that activated microglia are not sufficient for recruiting neutrophils with damage of this magnitude. This could mean that a minimum threshold of neural damage must be met before neutrophils will respond to damage of this type. Such a strategy would benefit the CNS. It is possible that resident microglia facilitate the necessary phagocytic and retinal remodeling response despite release of cytokines from damaged retinal cells that would normally recruit systemic immune cells in peripheral tissues.

Future work will explore whether there is a threshold magnitude of neuronal cell loss required for recruitment of systemic cells that is unique to the retina. Building on this work, next studies will examine more severe or widespread injury regimes that may provide stronger activating molecular signals and interact with a larger population of systemic cells.

Microglia may inhibit neutrophil activation

Microglia may be involved in a system that protects the CNS from propagating a much larger systemic response, potentially exacerbating disease pathologies that would compromise overall CNS function. From this work, both *in vivo* and *ex vivo* data corroborate the finding that microglia become reactive, whereas no evidence of neutrophil recruitment is observed. In another damage model[87], they report that tissue-resident macrophages may exhibit the capacity to cloak tissue micro-damage. This offers the possibility that resident immune cells, such as retinal microglia, can handle small insults without inducing a chemokine cascade that may invoke a larger systemic response that could further damage the precious retinal tissue.[88] Regardless of the mechanism, we find that despite a robust microglial activation that lasts for weeks, at no time point do they recruit neutrophils. The nuance of this interaction likely represents the fine balance that facilitates a helpful local response within the CNS that does not impart a more widespread cytokine storm that may otherwise exacerbate retinal damage. Further work will explore whether microglia exhibit a cloaking response in the retina, inhibiting neutrophil or other immune cell extravasation/chemotaxis toward

lesion sites. We expect such work to be pivotal in understanding the balance that is broken or left unchecked in conditions of autoimmune disease and the umbrella of diseases that comprise the uveitic response which is a direct threat to lifelong vision.[89]

Conclusion

Here, we have applied innovative *in vivo* imaging at the microscopic scale to reveal the cellular immune response to a retina in jeopardy. The dynamic environment of the retina includes a native population of resident microglia and systemic immune cells delivered through the vasculature. These two lines of defense work in concert in the mammalian body and are critical for maintaining retinal homeostasis. In this work we directly study the interaction between microglia and neutrophils, two major classes of immune cells that are implicated in inflammatory initiation, escalation, propagation and debris removal in response to an acute geographical injury in the retina. Using cutting-edge retinal imaging modalities, we find that resident microglia become locally activated and regionally responsive to focal laser lesion. Cells migrate away from their stratified locations near plexiform layers of the retina and migrate toward the axial site of damage within hours to weeks after injury. However, systemic neutrophils, which are typically regarded as first-line responders to tissue damage, are not recruited to this damage despite neutrophils flowing within 10s of microns away from the location of damage (Figure 8 – video 2). Beyond the context of this specific finding, we share this work with the excitement that AOSLO cellular level imaging

may reveal the interaction of multiple immune cell types in the living retina, a unique tissue in its own regard. By using fluorophores associated with specific immune cell populations, the complex immune cell dynamics that orchestrate the immune response may be examined in this specialized tissue and may reveal further insights to the interactions of single immune cells in the living body in a non-invasive way.

Acknowledgements: Thanks to Colin Chu**,** Justin Elstrott and Tiffany Heaster for useful intellectual conversations. Thanks to Minsoo Kim for generously transferring the Catchup mouse strain.

References:

1. Stone, J. *et al.* Mechanisms of photoreceptor death and survival in mammalian retina. *Progress in Retinal and Eye Research* **18**, 689–735 (1999).
2. García-Ayuso, D., Di Pierdomenico, J., Vidal-Sanz, M. & Villegas-Pérez, M. P. Retinal Ganglion Cell Death as a Late Remodeling Effect of Photoreceptor Degeneration. *Int J Mol Sci* **20**, 4649 (2019).
3. Boycott, B. B. & Hopkins, J. M. Microglia in the retina of monkey and other mammals: its distinction from other types of glia and horizontal cells. *Neuroscience* **6**, 679–688 (1981).
4. Silverman, S. M. & Wong, W. T. Microglia in the Retina: Roles in Development, Maturity, and Disease. *Annual Review of Vision Science* **4**, 45–77 (2018).
5. Wang, X. *et al.* Requirement for Microglia for the Maintenance of Synaptic Function and Integrity in the Mature Retina. *J. Neurosci.* **36**, 2827–2842 (2016).
6. Zhang, Y. *et al.* Repopulating retinal microglia restore endogenous organization and function under CX3CL1-CX3CR1 regulation. *Science Advances* **4**, eaap8492 (2018).
7. Joseph, A. *et al.* Imaging the dynamics of individual processes of microglia in the living retina in vivo. *Biomed. Opt. Express, BOE* **12**, 6157–6183 (2021).
8. Nimmerjahn, A., Kirchhoff, F. & Helmchen, F. Resting microglial cells are highly dynamic surveillants of brain parenchyma in vivo. *Science* **308**, 1314–1318 (2005).
9. Neumann, H., Kotter, M. R. & Franklin, R. J. M. Debris clearance by microglia: an essential link between degeneration and regeneration. *Brain* **132**, 288 (2009).
10. Zabel, M. K. *et al.* Microglial phagocytosis and activation underlying photoreceptor degeneration is regulated by CX3CL1-CX3CR1 signaling in a mouse model of retinitis pigmentosa. *Glia* **64**, 1479–1491 (2016).

740 11. Tremblay, M.-È. & Majewska, A. K. A role for microglia in synaptic plasticity? *Commun Integr*
741 *Biol* **4**, 220–222 (2011).
742 12. Sipe, G. O. *et al.* Microglial P2Y12 is necessary for synaptic plasticity in mouse visual cortex.
743 *Nat Commun* **7**, 10905 (2016).
744 13. Márquez-Ropero, M., Benito, E., Plaza-Zabala, A. & Sierra, A. Microglial Corpse Clearance:
745 Lessons From Macrophages. *Front Immunol* **11**, 506 (2020).
746 14. Karlen, S. J., Miller, E. B. & Burns, M. E. Microglia Activation and Inflammation During the
747 Death of Mammalian Photoreceptors. *Annual Review of Vision Science* **6**, 149–169 (2020).
748 15. Okunuki, Y. *et al.* Retinal microglia initiate neuroinflammation in ocular autoimmunity. *Proc*
749 *Natl Acad Sci U S A* **116**, 9989–9998 (2019).
750 16. Kremlev, S. G., Roberts, R. L. & Palmer, C. Differential expression of chemokines and
751 chemokine receptors during microglial activation and inhibition. *Journal of*
752 *Neuroimmunology* **149**, 1–9 (2004).
753 17. Babcock, A. A., Kuziel, W. A., Rivest, S. & Owens, T. Chemokine Expression by Glial Cells
754 Directs Leukocytes to Sites of Axonal Injury in the CNS. *J. Neurosci.* **23**, 7922–7930 (2003).
755 18. Boyce, M. *et al.* Microglia–Neutrophil Interactions Drive Dry AMD-like Pathology in a Mouse
756 Model. *Cells* **11**, 3535 (2022).
757 19. Zhou, H., Lapointe, B. M., Clark, S. R., Zbytnuik, L. & Kubes, P. A Requirement for Microglial
758 TLR4 in Leukocyte Recruitment into Brain in Response to Lipopolysaccharide. *The Journal of*
759 *Immunology* **177**, 8103–8110 (2006).
760 20. physiological_data_000664.pdf. https://www.jax.org/-/media/jaxweb/files/jax-mice-and-
761 services/physiological_data_000664.pdf (2007).

762 21. Burn, G. L., Foti, A., Marsman, G., Patel, D. F. & Zychlinsky, A. The Neutrophil. *Immunity* **54**,
763 1377–1391 (2021).
764 22. Peiseler, M. & Kubes, P. More friend than foe: the emerging role of neutrophils in tissue
765 repair. *J Clin Invest* **129**, 2629–2639 (2019).
766 23. Kraus, R. F. & Gruber, M. A. Neutrophils—From Bone Marrow to First-Line Defense of the
767 Innate Immune System. *Front Immunol* **12**, 767175 (2021).
768 24. Joseph, A., Chu, C. J., Feng, G., Dholakia, K. & Schallek, J. Label-free imaging of immune cell
769 dynamics in the living retina using adaptive optics. *eLife* **9**, e60547 (2020).
770 25. Sulai, Y. N., Scoles, D., Harvey, Z. & Dubra, A. Visualization of retinal vascular structure and
771 perfusion with a nonconfocal adaptive optics scanning light ophthalmoscope. *J Opt Soc Am*
772 *A Opt Image Sci Vis* **31**, 569–579 (2014).
773 26. Guevara-Torres, A., Williams, D. R. & Schallek, J. B. Origin of cell contrast in offset aperture
774 adaptive optics ophthalmoscopy. *Opt. Lett., OL* **45**, 840–843 (2020).
775 27. Chui, T. Y. P., VanNasdale, D. A. & Burns, S. A. The use of forward scatter to improve retinal
776 vascular imaging with an adaptive optics scanning laser ophthalmoscope. *Biomedical Optics*
777 *Express* **3**, 2537 (2012).
778 28. Geng, Y. *et al.* Optical properties of the mouse eye. *Biomed. Opt. Express* **2**, 717–738 (2011).
779 29. Geng, Y. *et al.* Adaptive optics retinal imaging in the living mouse eye. *Biomed. Opt. Express*
780 **3**, 715–734 (2012).
781 30. Guevara-Torres, A., Joseph, A. & Schallek, J. B. Label free measurement of retinal blood cell
782 flux, velocity, hematocrit and capillary width in the living mouse eye. *Biomed. Opt. Express,*
783 *BOE* **7**, 4228–4249 (2016).

784 31. Joseph, A. *et al.* Label-free tracking of single blood cells in the retinal immune response.
785 *Journal of Vision* **19**, 20–20 (2019).
786 32. Joseph, A., Guevara-Torres, A. & Schallek, J. Imaging single-cell blood flow in the smallest to
787 largest vessels in the living retina. *eLife* **8**, e45077 (2019).
788 33. Guevara-Torres, A., Williams, D. R. & Schallek, J. B. Imaging translucent cell bodies in the
789 living mouse retina without contrast agents. *Biomedical Optics Express* **6**, 2106 (2015).
790 34. Schallek, J., Geng, Y., Nguyen, H. & Williams, D. R. Morphology and topography of retinal
791 pericytes in the living mouse retina using in vivo adaptive optics imaging and ex vivo
792 characterization. *Invest. Ophthalmol. Vis. Sci.* **54**, 8237–8250 (2013).
793 35. Pinhas, A. *et al.* In vivo imaging of human retinal microvasculature using adaptive optics
794 scanning light ophthalmoscope fluorescein angiography. *Biomed Opt Express* **4**, 1305–1317
795 (2013).
796 36. Chu, C. J. *et al.* Multimodal analysis of ocular inflammation using the endotoxin-induced
797 uveitis mouse model. *Disease Models & Mechanisms* **9**, 473–481 (2016).
798 37. Hasenberg, A. *et al.* Catchup: a mouse model for imaging-based tracking and modulation of
799 neutrophil granulocytes. *Nat Methods* **12**, 445–452 (2015).
800 38. Crane, I. J. & Liversidge, J. Mechanisms of leukocyte migration across the blood–retina
801 barrier. *Semin Immunopathol* **30**, 165–177 (2008).
802 39. Xu, H. *et al.* Involvement of CD44 in leukocyte trafficking at the blood-retinal barrier. *Journal
803 of Leukocyte Biology* **72**, 1133–1141 (2002).
804 40. Xu, H. *et al.* Reduction in shear stress, activation of the endothelium, and leukocyte priming
805 are all required for leukocyte passage across the blood—retina barrier. *Journal of Leukocyte
806 Biology* **75**, 224–232 (2004).

807 41. Rosenbaum, J. T., McDevitt, H. O., Guss, R. B. & Egbert, P. R. Endotoxin-induced uveitis in
808 rats as a model for human disease. *Nature* **286**, 611–613 (1980).
809 42. Dubra, A. & Harvey, Z. Registration of 2D Images from Fast Scanning Ophthalmic
810 Instruments. in *Biomedical Image Registration* (eds. Fischer, B., Dawant, B. M. & Lorenz, C.)
811 60–71 (Springer, Berlin, Heidelberg, 2010). doi:10.1007/978-3-642-14366-3_6.
812 43. Yang, Q. *et al.* Closed-loop optical stabilization and digital image registration in adaptive
813 optics scanning light ophthalmoscopy. *Biomedical Optics Express* **5**, 3174 (2014).
814 44. Fiji: an open-source platform for biological-image analysis | Nature Methods.
815 https://www.nature.com/articles/nmeth.2019.
816 45. Joseph, A., Guevara-Torres, A., Williams, D. R. & Schallek, J. B. Measurement of blood flow
817 in the largest vessels and smallest capillaries in the living mouse retina using an adaptive
818 optics scanning light ophthalmoscope. *Invest. Ophthalmol. Vis. Sci.* **56**, 3323–3323 (2015).
819 46. Dholakia, K., Guevara-Torres, A. & Schallek, J. B. Early changes in blood cell flux in retinal
820 capillaries of diabetic and healthy mice imaged in vivo. *Invest. Ophthalmol. Vis. Sci.* **61**, 806–
821 806 (2020).
822 47. Feng, G. *et al.* High-resolution structural and functional retinal imaging in the awake
823 behaving mouse. *Commun Biol* **6**, 1–15 (2023).
824 48. Carter-Dawson, L. D. & LaVail, M. M. Rods and cones in the mouse retina. I. Structural
825 analysis using light and electron microscopy. *J. Comp. Neurol* **188**, 245–262 (1979).
826 49. Jeon, C. J., Strettoi, E. & Masland, R. H. The major cell populations of the mouse retina. *J*
827 *Neurosci* **18**, 8936–8946 (1998).

828 50. Dholakia, K. Y., Guevara-Torres, A., Feng, G., Power, D. & Schallek, J. In Vivo Capillary
829 Structure and Blood Cell Flux in the Normal and Diabetic Mouse Eye. *Invest Ophthalmol Vis*
830 *Sci* **63**, 18 (2022).
831 51. Wahl, D. J., Ng, R., Ju, M. J., Jian, Y. & Sarunic, M. V. Sensorless adaptive optics multimodal
832 en-face small animal retinal imaging. *Biomed Opt Express* **10**, 252–267 (2019).
833 52. Puthenparampil, M. *et al.* Hyper-Reflecting Foci in Multiple Sclerosis Retina Associate With
834 Macrophage/Microglia-Derived Cytokines in Cerebrospinal Fluid. *Front Immunol* **13**, 852183
835 (2022).
836 53. Pilotto, E. *et al.* Hyper-reflective retinal foci as possible in vivo imaging biomarker of
837 microglia activation in von Hippel-Lindau disease. *PLoS One* **17**, e0272318 (2022).
838 54. Kornmann, L. M. *et al.* Echogenic perfluorohexane-loaded macrophages adhere in vivo to
839 activated vascular endothelium in mice, an explorative study. *Cardiovasc Ultrasound* **13**, 1
840 (2015).
841 55. Paques, M. *et al.* Structural and hemodynamic analysis of the mouse retinal
842 microcirculation. *Invest. Ophthalmol. Vis. Sci* **44**, 4960–4967 (2003).
843 56. Stahl, A. *et al.* The Mouse Retina as an Angiogenesis Model. *Investigative Ophthalmology &*
844 *Visual Science* **51**, 2813–2826 (2010).
845 57. Senut, M.-C., Gulati-Leekha, A. & Goldman, D. An Element in the α1-Tubulin Promoter Is
846 Necessary for Retinal Expression during Optic Nerve Regeneration But Not after Eye Injury
847 in the Adult Zebrafish. *J. Neurosci.* **24**, 7663–7673 (2004).
848 58. Maidana, D. E., Gonzalez-Buendia, L., Miller, J. W. & Vavvas, D. G. Local photoreceptor cell
849 death differences in the murine model of retinal detachment. *Sci Rep* **11**, 18798 (2021).

850 59. Wan, J. *et al.* Preferential regeneration of photoreceptor from Müller glia after retinal
851 degeneration in adult rat. *Vision Research* **48**, 223–234 (2008).
852 60. Rösch, S. *et al.* The effects of iodoacetic acid on the mouse retina. *Graefes Arch Clin Exp*
853 *Ophthalmol* **253**, 25–35 (2015).
854 61. Nimmerjahn, A., Kirchhoff, F. & Helmchen, F. Resting microglial cells are highly dynamic
855 surveillants of brain parenchyma in vivo. *Science* **308**, 1314–1318 (2005).
856 62. Davalos, D. *et al.* ATP mediates rapid microglial response to local brain injury in vivo. *Nat*
857 *Neurosci* **8**, 752–758 (2005).
858 63. Shah, R. S., Soetikno, B. T., Lajko, M. & Fawzi, A. A. A Mouse Model for Laser-induced
859 Choroidal Neovascularization. *J Vis Exp* 53502 (2015) doi:10.3791/53502.
860 64. Khan, A. H. *et al.* A laser-induced mouse model of progressive retinal degeneration with
861 central sparing displays features of parafoveal geographic atrophy. *Sci Rep* **13**, 4194 (2023).
862 65. Strazzeri, J. M. *et al.* Focal damage to macaque photoreceptors produces persistent visual
863 loss. *Exp Eye Res* **119**, 88–96 (2014).
864 66. Dhakal, K. R. *et al.* Localized Photoreceptor Ablation Using Femtosecond Pulses Focused
865 With Adaptive Optics. *Transl Vis Sci Technol* **9**, 16 (2020).
866 67. Schwarz, C. *et al.* Selective S Cone Damage and Retinal Remodeling Following Intense
867 Ultrashort Pulse Laser Exposures in the Near-Infrared. *Investigative Ophthalmology & Visual*
868 *Science* **59**, 5973–5984 (2018).
869 68. Calford, M. B., Schmid, L. M. & Rosa, M. G. P. Monocular focal retinal lesions induce short–
870 term topographic plasticity in adult cat visual cortex. *Proceedings of the Royal Society of*
871 *London. Series B: Biological Sciences* **266**, 499–507 (1999).

872 69. Dreher, B., Burke, W. & Calford, M. B. Chapter 15 Cortical plasticity revealed by
873 circumscribed retinal lesions or artificial scotomas. in *Progress in Brain Research* vol. 134
874 217–246 (Elsevier, 2001).
875 70. Vitellas, C. *et al.* CONE PHOTORECEPTOR INTEGRITY ASSESSED WITH ADAPTIVE OPTICS
876 IMAGING AFTER LASER POINTER-INDUCED RETINAL INJURY. *Retinal Cases and Brief Reports*
877 **16**, 586 (2022).
878 71. Linton, E. *et al.* Retinal burns from laser pointers: a risk in children with behavioural
879 problems. *Eye* **33**, 492–504 (2019).
880 72. Current ROP Therapies: How Laser and Anti-VEGF Compare. *American Academy of*
881 *Ophthalmology* https://www.aao.org/eyenet/article/current-rop-therapies-how-laser-
882 antivegf-compare (2014).
883 73. Reddy, S. V. & Husain, D. Panretinal Photocoagulation: A Review of Complications. *Semin*
884 *Ophthalmol* **33**, 83–88 (2018).
885 74. Haupert, C. L. *et al.* Optimal laser power to rupture Bruch's membrane and the retinal vein
886 in the pig. *Ophthalmic Surg Lasers Imaging* **34**, 122–127 (2003).
887 75. Shah, R. S., Soetikno, B. T., Lajko, M. & Fawzi, A. A. A Mouse Model for Laser-induced
888 Choroidal Neovascularization. *J Vis Exp* e53502 (2015) doi:10.3791/53502.
889 76. Ley, K., Laudanna, C., Cybulsky, M. I. & Nourshargh, S. Getting to the site of inflammation:
890 the leukocyte adhesion cascade updated. *Nat Rev Immunol* **7**, 678–689 (2007).
891 77. Busch, E. M., Gorgels, T. G. & Van Norren, D. Filling-in after focal loss of photoreceptors in
892 rat retina. *Exp Eye Res* **68**, 485–492 (1999).

893 78. Lee, J. E., Liang, K. J., Fariss, R. N. & Wong, W. T. Ex vivo Dynamic Imaging of Retinal
894 Microglia using Time-lapse Confocal Microscopy. *Invest Ophthalmol Vis Sci* **49**, 4169–4176
895 (2008).
896 79. Miller, E. B., Zhang, P., Ching, K., Pugh, E. N. & Burns, M. E. In vivo imaging reveals transient
897 microglia recruitment and functional recovery of photoreceptor signaling after injury.
898 *Proceedings of the National Academy of Sciences* **116**, 16603–16612 (2019).
899 80. Wu, C. Y. *et al.* Acute Solar Retinopathy Imaged With Adaptive Optics, Optical Coherence
900 Tomography Angiography, and En Face Optical Coherence Tomography. *JAMA*
901 *Ophthalmology* **136**, 82–85 (2018).
902 81. Allen, C. *et al.* Neutrophil Cerebrovascular Transmigration Triggers Rapid Neurotoxicity
903 through Release of Proteases Associated with Decondensed DNA. *The Journal of*
904 *Immunology* **189**, 381–392 (2012).
905 82. Panda-Jonas, S., Jonas, J. B. & Jakobczyk-Zmija, M. Retinal Photoreceptor Density Decreases
906 with Age. *Ophthalmology* **102**, 1853–1859 (1995).
907 83. Margalit, E. & Sadda, S. R. Retinal and Optic Nerve Diseases. *Artificial Organs* **27**, 963–974
908 (2003).
909 84. Sadik, C. D., Kim, N. D. & Luster, A. D. Neutrophils cascading their way to inflammation.
910 *Trends Immunol* **32**, 452–460 (2011).
911 85. Worthen, G. S. *et al.* Neutrophil-mediated pulmonary vascular injury. Synergistic effect of
912 trace amounts of lipopolysaccharide and neutrophil stimuli on vascular permeability and
913 neutrophil sequestration in the lung. *Am Rev Respir Dis* **136**, 19–28 (1987).
914 86. Linas, S. L., Whittenburg, D., Parsons, P. E. & Repine, J. E. Mild renal ischemia activates
915 primed neutrophils to cause acute renal failure. *Kidney Int* **42**, 610–616 (1992).

916 87. Uderhardt, S., Martins, A. J., Tsang, J. S., Lämmermann, T. & Germain, R. N. Resident
917 Macrophages Cloak Tissue Microlesions to Prevent Neutrophil-Driven Inflammatory
918 Damage. *Cell* **177**, 541-555.e17 (2019).
919 88. Pfeifer, C. W. *et al.* Dysregulated CD200-CD200R signaling in early diabetes modulates
920 microglia-mediated retinopathy. *Proceedings of the National Academy of Sciences* **120**,
921 e2308214120 (2023).
922 89. Miserocchi, E., Fogliato, G., Modorati, G. & Bandello, F. Review on the Worldwide
923 Epidemiology of Uveitis. *European Journal of Ophthalmology* **23**, 705–717 (2013).
924
925

Figures & videos:

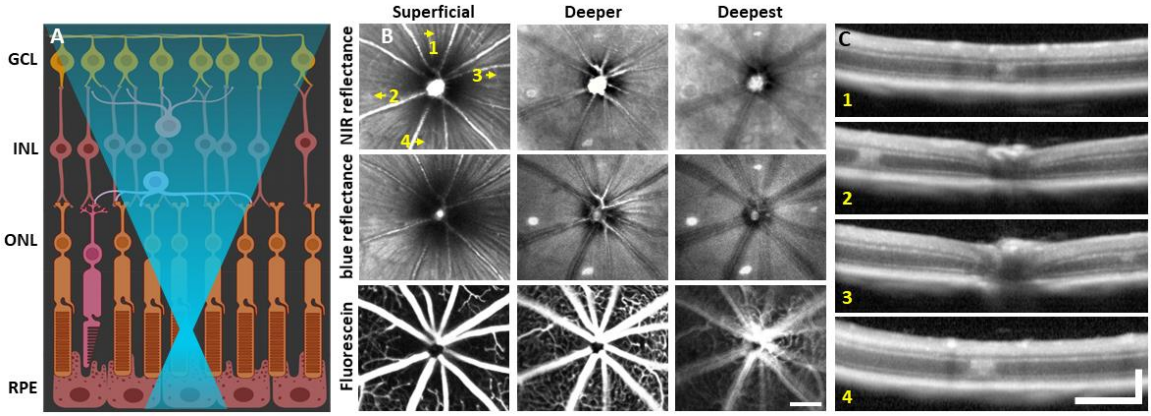

Figure 1. Laser injury assessed with commercial SLO and OCT. **(A)** 488 nm light is focused onto the photoreceptor outer segments using AOSLO. Created with Biorender.com. **(B)** 30° SLO images of NIR reflectance, blue reflectance and fluorescein angiography of a mouse retina 1 day after laser exposure. Three focal planes are shown. NIR and blue reflectance reveal small hyperreflective regions below the superficial plane. Fluorescein reveals intact vasculature with no sign of leakage. Arrows indicate regions with imparted laser damage (1-4). **(C)** OCT B-scans passing through laser-exposed regions indicated in B. Exposures produced a focal hyperreflective band within the ONL with adjacent retina appearing healthy. OCT images were spatially averaged (~30 µm, 3 B-scans). Scale bars = 200 µm horizontal, 200 µm vertical.

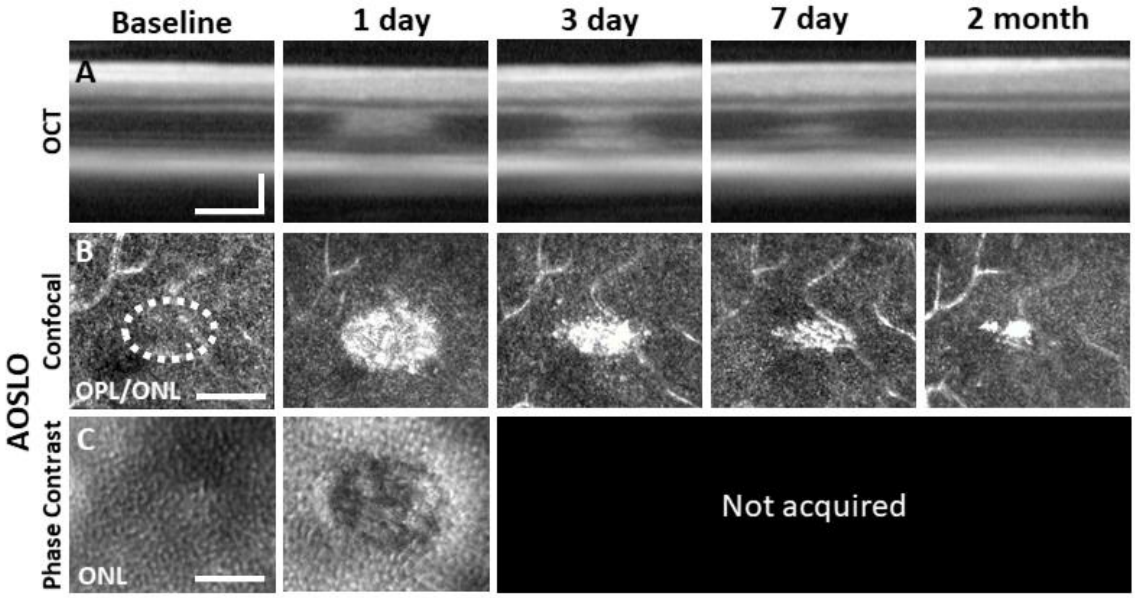

Figure 2. Laser damage temporally tracked with AOSLO and OCT. Laser-exposed retina was tracked with OCT **(A)**, confocal **(B)** and phase-contrast **(C)** AOSLO for baseline, 1, 3, 7 day and 2 month time points. OCT and confocal AOSLO display a hyperreflective phenotype that was largest/brightest at 1 day and became nearly invisible by 2 months. Dashed oval indicates region targeted for laser injury. Phase-contrast AOSLO revealed disrupted photoreceptor soma's 1 day after laser injury. OCT images were spatially averaged (~30 µm, 8 B-scans). Scale bars = 40 µm, OCT image vertical scale bar = 100 µm.

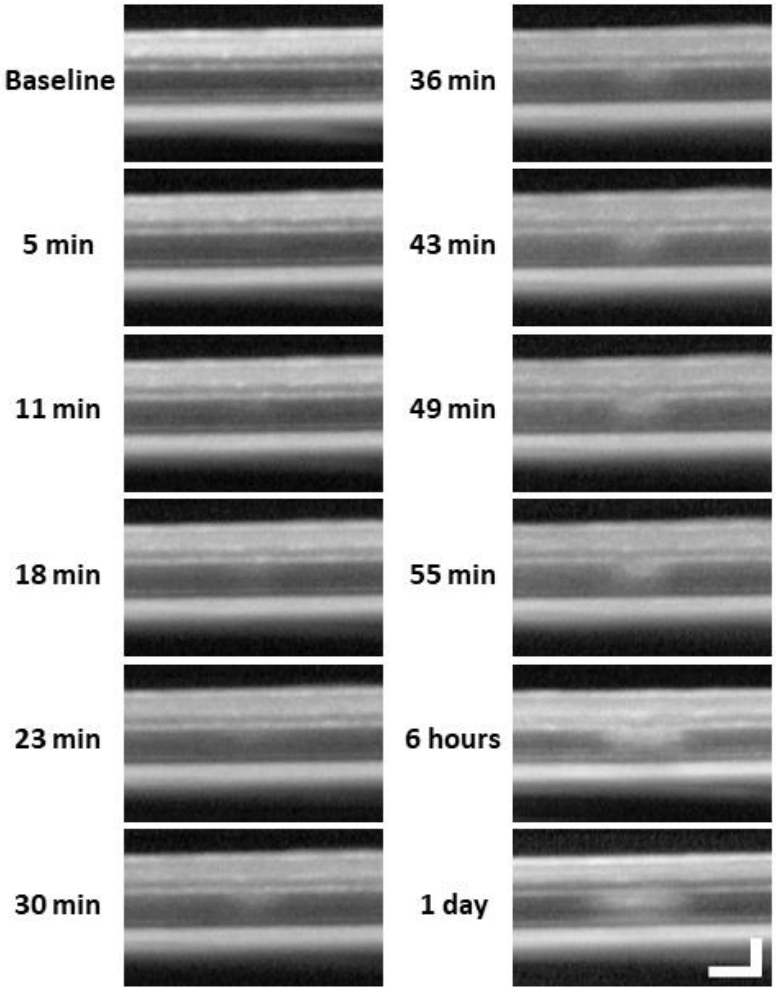

Figure 2 - figure supplement 1 Lesion location tracked from minutes to 1 day with OCT. After baseline OCT acquisition, OCT was performed every 5-7 minutes for one hour after 488 nm light exposure. 6 hour and 1 day time points were subsequently acquired. A band of hyperreflectivity forms near the OPL/ONL interface within 30 minutes of 488 nm light exposure. Hyperreflective band, spreads deeper into the ONL within ~1 hour. OCT images were spatially averaged (~30 μm, 8 B-scans). Scale bar = 40 μm horizontal, 100 μm vertical.

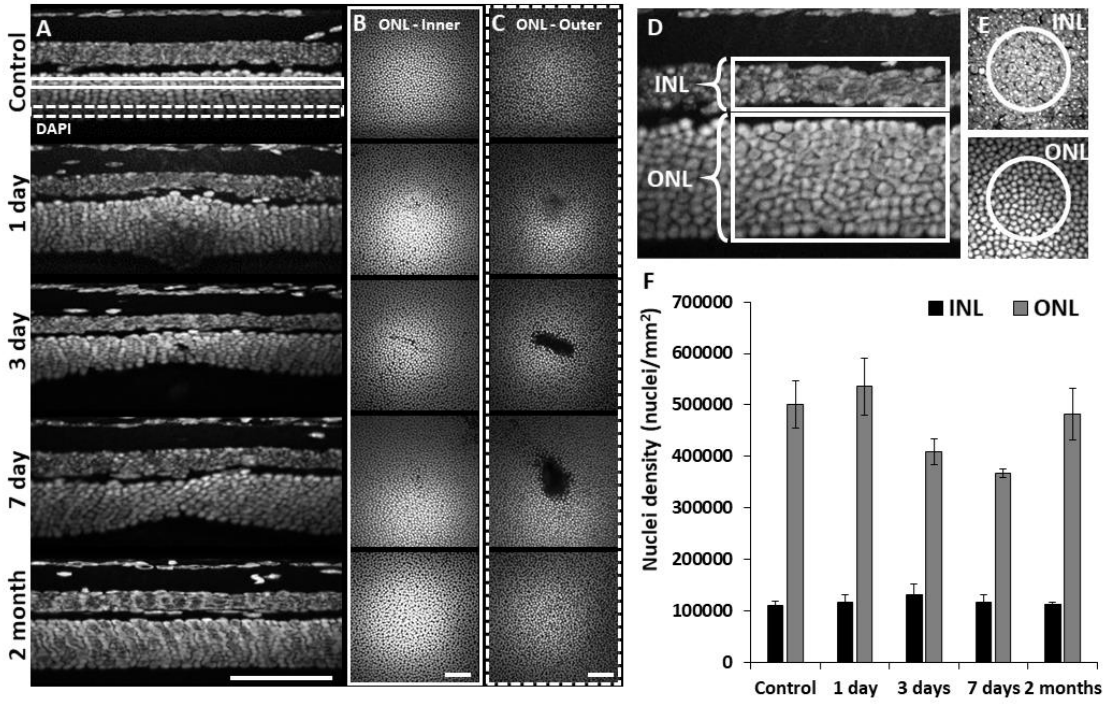

Figure 3. Retinal histology confirms photoreceptor ablation and preservation of inner retinal cells. Cross sectional view **(A)** and en-face **(B+C)** images of DAPI-stained whole-mount retinas (5 mice) at laser injury locations over time. By 1 day, ONL becomes thicker at lesion location, but thinner by 3 and 7 days. By 2 months, the ONL appeared similar to that of control. The inner (**B**, solid rectangle) and outer (**C**, dashed rectangle) stratum of ONL show axial differences in ONL loss**.** Most cell loss was seen in the outer aspect of the ONL **(C)**. Scale bars = 40 µm. **(D)** Cross section of DAPI-stained retina displaying INL and ONL regions for quantification. Each analysis region was 50 µm across and encompassed the entire INL or ONL. **(E)** En-face images show 50 µm diameter circles used for analysis. **(F)** Nuclei density for control and post-injury time points. ONL nuclei were reduced at 3 and 7 days ($p = 0.17$ and 0.07 respectively) while INL density remained stable ($n = 10$ mice, 3 unique regions per time point). Error bars display mean ± 1 SD.

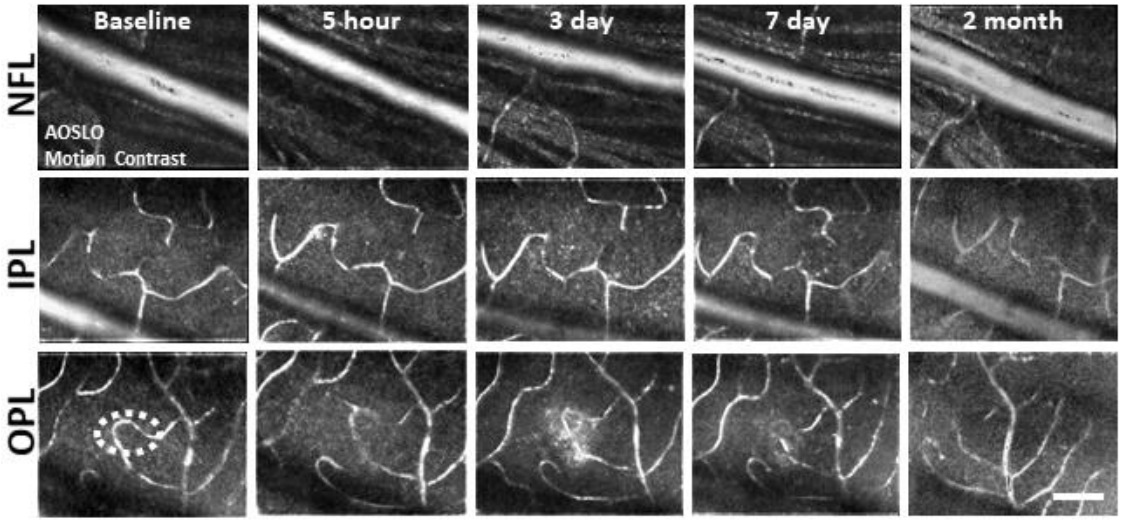

Figure 4. Microvascular perfusion unchanged after laser damage. A single location tracked over time and at three vascular plexuses using AOSLO. Motion-contrast images were generated from confocal videos to reveal vascular perfusion status. Retinal vasculature remained perfused for all time points tracked and at all depths. White oval indicates damage location. Scale bar = 40 µm.

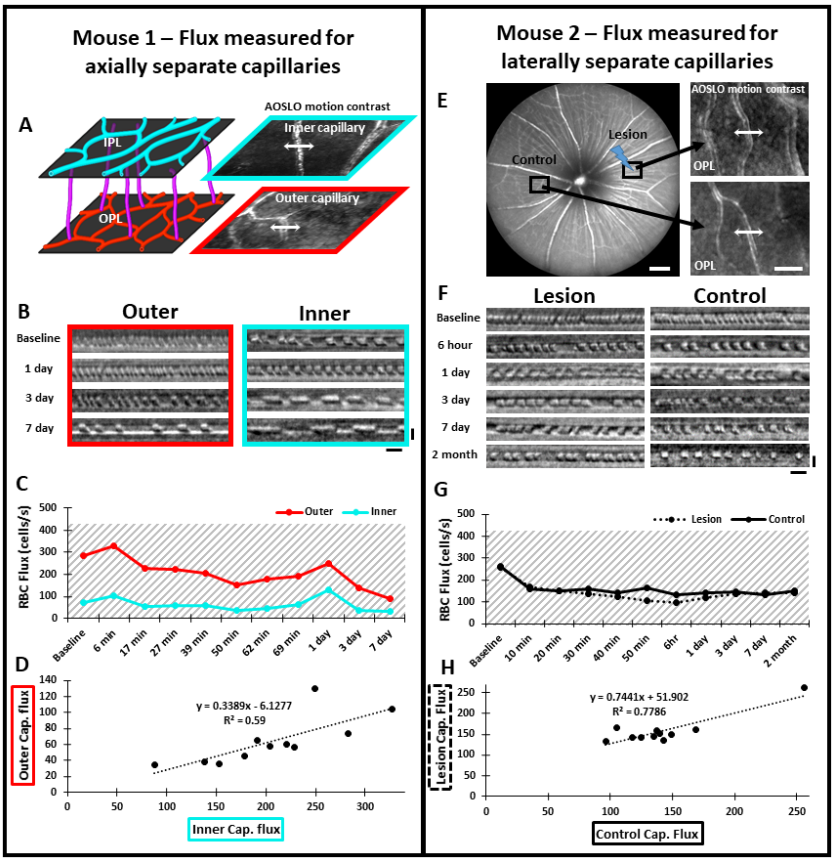

Figure 4 – figure supplement 1 Measurement of single-cell blood flux after laser damage using phase contrast AOSLO. **Mouse 1: (A)** The vascular plexus corresponding to IPL (cyan) and OPL (red) were targeted for flux determination. Blood cell flux was measured for 2 capillaries within the same field, at different depths. Arrows show the location for repeated line scan acquisitions. **(B)** RBC flux images were tracked up to 7 days post-damage. Scale bars = 10 ms, horizontal and 5 µm vertical. **(C)** Capillary flux measurements over 7 days. Despite the outer capillary displaying higher flux, both inner and outer capillaries changed synchronously for each time point. **(D)** Correlation of inner and outer capillary flux. Linear regression model displays a weak positive correlation (black dotted line). **Mouse 2: (E)** Left: Representative 55° SLO image showing regions targeted for capillary flux measurement. One region was subject to 488 nm laser damage and the other was left unlasered (Control). Scale bar = 200 µm. Right: Capillaries targeted for blood cell flux measurement. Arrows show the location for repeated line scan acquisitions. Scale bar = 40 µm. **(F)** RBC flux images were tracked up to 2 months post-damage. Scale bars = 10 ms horizontal and 5 µm vertical. **(G)** Capillary flux remained similar at lesion and control locations over all time points assessed. Gray shaded regions indicate range for normal capillary flux in the healthy C57BL/6J mouse (Dholakia et al 2022). **(H)** Correlation of flux in lesion and control locations. Linear regression model displays a positive correlation (black dotted line).

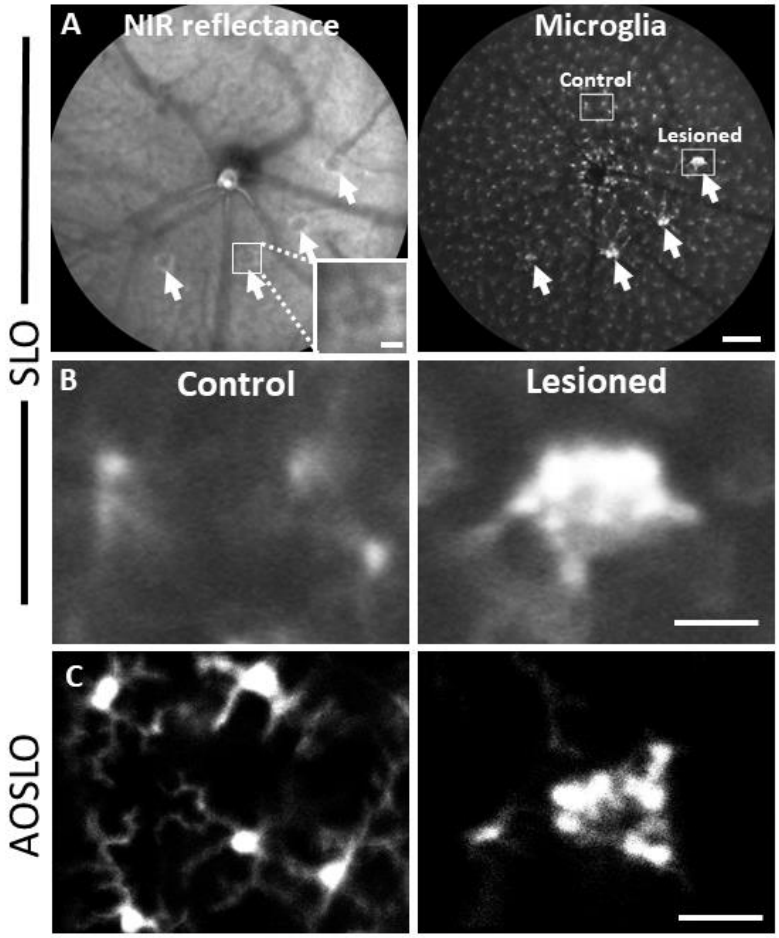

Figure 5. Microglial response 1 day after laser injury imaged in vivo with fluorescence SLO and AOSLO. **(A)** Left: Deep-focus NIR SLO fundus image (55˚ FOV) of laser-injured retina. White arrowheads point to damaged locations showing hyperreflective regions. Inset scale bar = 40 µm. Right: Fluorescence fundus image from same location. Fluorescent CX3CR1-GFP microglia are distributed across the retina and show congregations at laser-damaged locations. Scale bar = 200 µm. **(B)** Magnified SLO images of microglia at laser-damaged and control locations (indicated in A, right, white boxes). Control location displays distributed microglial whereas microglia at the lesion location are bright and focally aggregated. **(C)** Fluorescence AOSLO images show greater detail of cell morphology at the same scale. In control locations microglia showed ramified morphology and distributed concentration whereas damage locations revealed dense aggregation of many microglia that display less ramification. Scale bars = 40 µm.

Refer to .avi file

Figure 5 – video 1 Dynamic pseudopodia imaged with phase-contrast AOSLO 1 day post-injury. At the OPL/ONL border, a putative microglial pseudopod extension was captured among a field of static, disrupted PR somas. Video is 3 minutes elapsed. Scale bars = 20 μm.

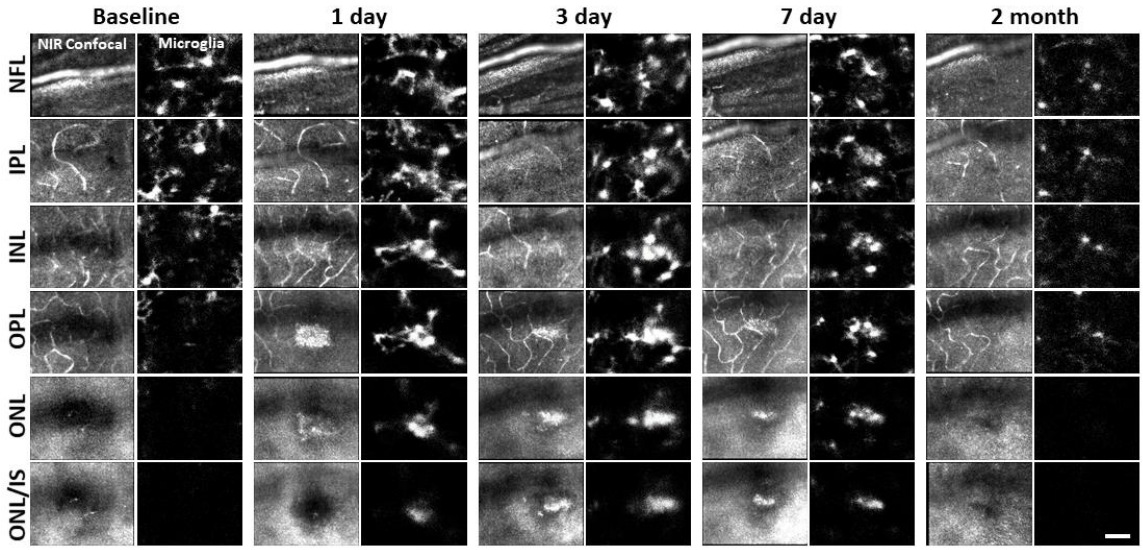

Figure 6. Microglial response to laser injury tracked with AOSLO. Simultaneously acquired NIR confocal and fluorescence AOSLO images across different retinal depths. Data are from one CX3CR1-GFP mouse tracked for 2 months. Microglia swarm to hyperreflective locations within 1 day. Microglia maintain an aggregated density for days and resolve by 2 months after damage. Scale bar = 40 µm.

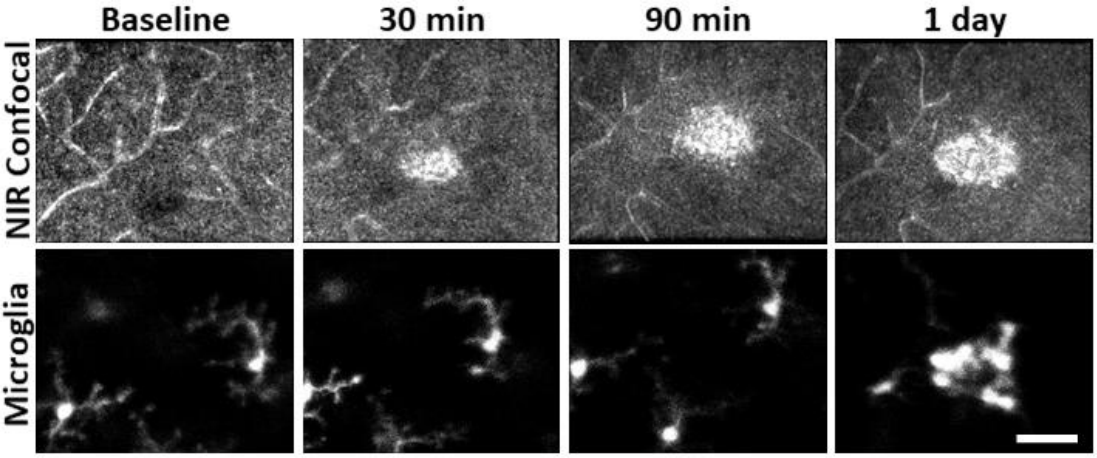

Figure 6 – figure supplement 1 Hyperreflective appearance emerges before microglia swarm to damage location. AOSLO confocal and fluorescence images were acquired for baseline, 30, 90 minute and 1 day post-laser exposure. The hyperreflective phenotype appeared within 30 minutes post damage. Microglia were not found to aggregate until ~1 day after. Scalebar = 40 μm.

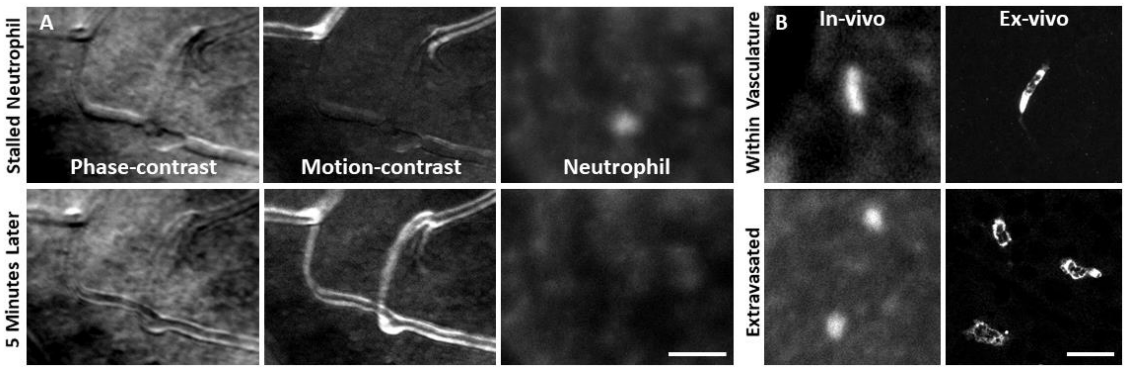

Figure 7. Neutrophil morphology imaged in vivo using AOSLO. **(A)** Phase-contrast, motion-contrast and fluorescence AOSLO reveal the impact of passing neutrophils on single capillaries. A rare and exemplary event shows a neutrophil transiently impeding capillary blood flow for minutes in healthy retina. Scale bar = 40 µm. **(B)** In-vivo AOSLO and ex-vivo fluorescence microscopy show neutrophils in two states. Neutrophils within capillaries displayed elongated, tubular morphology. Extravasated neutrophils were more spherical. Bottom images show extravasated neutrophils in response to LPS model for comparison (not laser damage model). Scale bar = 20 µm.

Refer to .avi file

Figure 7 – video 1 Neutrophil dynamics within a primary retinal vessel in a Catchup mouse. Confocal (left) and fluorescence (right) AOSLO were acquired from a large primary retinal vessel simultaneously. Several quickly flowing neutrophils are seen as streaks within the lumen of the large retinal vessel. Video plays in real-time (25 FPS, 20 seconds). Scale bar = 20 μm.

Refer to .avi file

Figure 7 – video 2 Neutrophils imaged in capillaries of a Catchup mouse. Motion-contrast (left) and fluorescence (right) AOSLO show a single neutrophil moving through a branch of the OPL capillary network. Red circles/arrows indicate neutrophil path within the vascular perfusion map. Rare neutrophils were found to move slowly through capillaries. Video is 0.4 seconds elapsed. Scale bar = 20 μm.

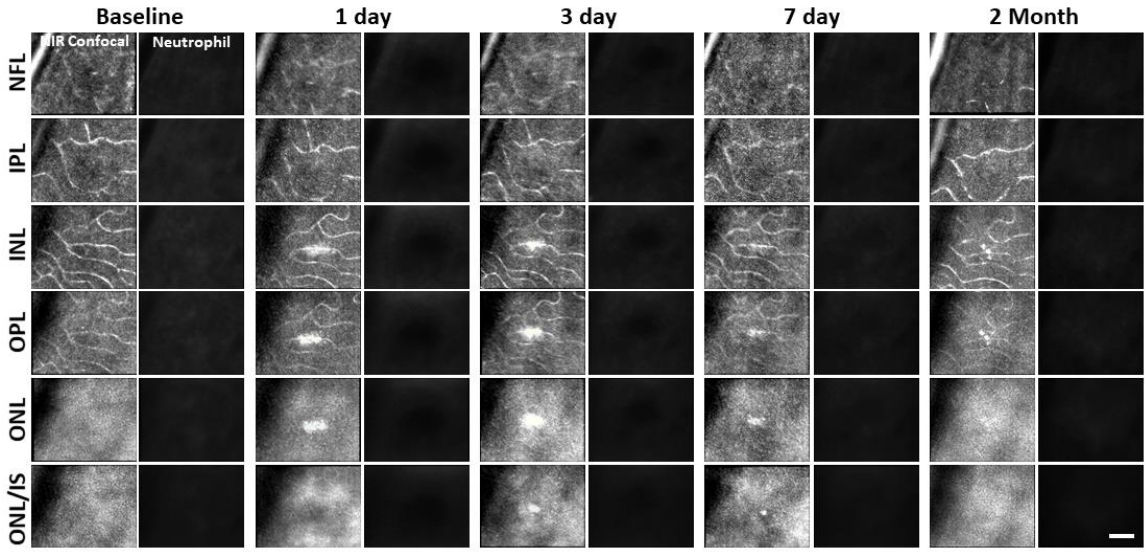

Figure 8. Retinal damage location tracked with AOSLO does not show accumulation of neutrophils. A single retinal location was tracked in a Catchup mouse from baseline to 2 months after lesion. Location of the lesion is apparent at 1 and 3 days post injury with diminishing visibility after 1 week. Despite the ability to detect neutrophils (Figure 7), we did not observe stalled, aggregated or an accumulation of neutrophils at any time point evaluated. This evaluation was confirmed at multiple depths ranging from the NFL to the ONL of the retina in vivo. Scale bar = 40 µm.

Refer to .avi file

Figure 8 – video 1 Neutrophil dynamics within a primary retinal vessel in a Catchup mouse 1 day after a deep retinal laser lesion is placed nearby. Confocal (left) and fluorescence (right) AOSLO images were acquired simultaneously. Quickly flowing neutrophils are seen as streaks within the lumen of this large retinal vessel and despite the adjacent deep retinal lesion (within 100 μm), there is no indication of rolling or crawling neutrophils. Video plays in real-time (25 FPS, 20 seconds). Scale bar = 20 μm.

Refer to .avi file

Figure 8 – video 2 Neutrophil dynamics within an OPL capillary in a Catchup mouse 1 day after deep laser injury. Motion-contrast (left) and fluorescence (right) AOSLO are displayed in tandem. At 1 day post-laser injury, a single neutrophil is seen moving through a capillary that runs directly through the injury site (yellow oval). Despite injury, neutrophil does not slow or stall at the lesion location. Video is 0.68 seconds elapsed. Scale bar = 20 μm.

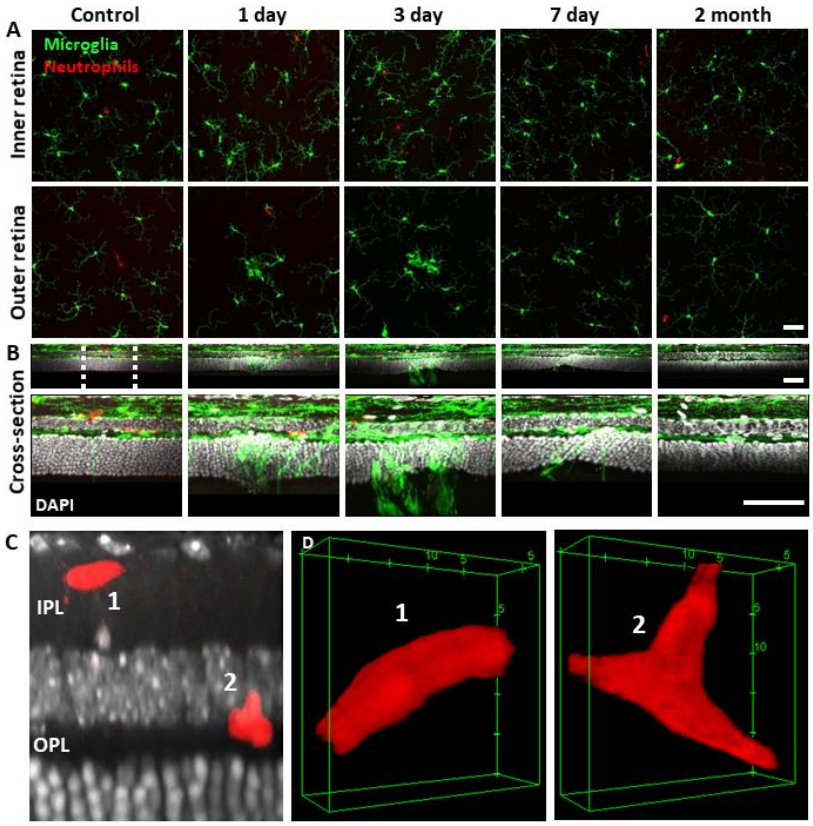

Figure 9. Neutrophil behavior under laser injury, as observed through ex vivo confocal microscopy, remains unresponsive despite marked microglial activation **(A)** En-face max intensity projection images of inner and outer (separated by approximate INL center) retinal microglia/neutrophils in Ly-6G-647-stained CX3CR1-GFP retinas. Microglia display focal aggregation in the outer retina for 1, 3 and 7 day time points that is resolved by 2 months. Neutrophils do not aggregate or colocalize to the injury location at any time point. Z-stacks were collected from 5 mice for the indicated time points. **(B)** Cross-sectional views of en-face z-stacks presented in A, including DAPI nuclear label. White dotted line indicates 100 µm region expanded below. Microglia migrate into the ONL by 1, 3 and 7 days post-laser injury and return to an axial distribution similar to that of control by 2 months. The few neutrophils detected remained within the inner retina. Scale bars = 40 µm. **(C)** Orthogonal view of DAPI-stained retina with Ly-6G-647-labelled overlay 1 day post-laser-injury. In a rare example, 2 neutrophils are found within the IPL/OPL layers despite a nearby outer retinal laser lesion. Scale bar = 20 µm. **(D)** Magnified 3D cubes representing cell 1 and 2 in C. Cell 1 displays pill-shaped morphology and cell 2 is localized to a putative capillary branch-point. Each are confined within vessels suggesting they do not extravasate in response to laser injury.

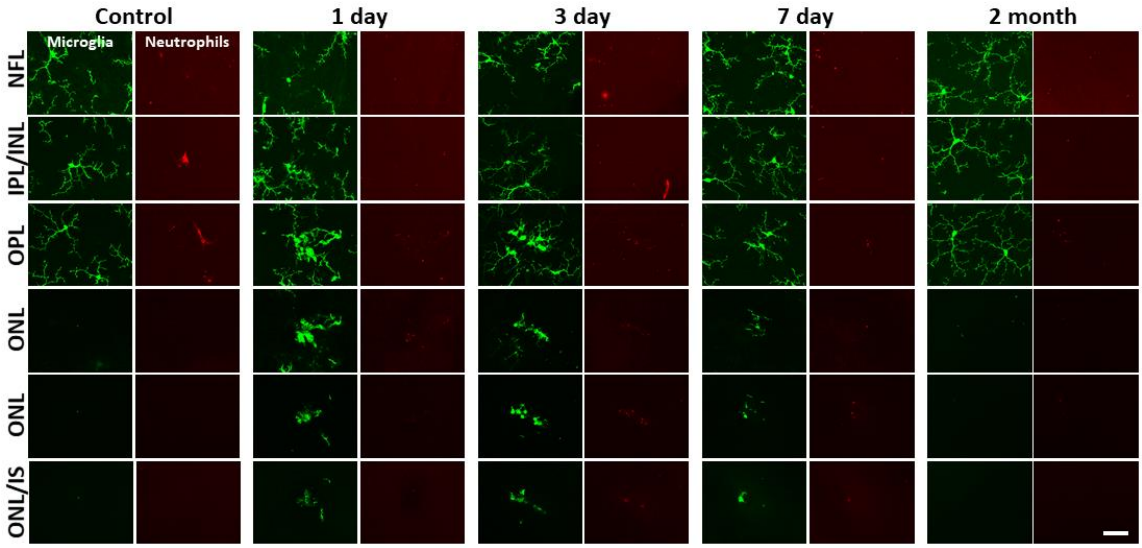

Figure 9 – figure supplement 1 Neutrophil/microglial response to laser injury tracked with *ex vivo* confocal microscopy. Simultaneously acquired GFP-positive microglia and Ly-6G-647-positive neutrophils were imaged with confocal microscopy in 5 CX3CR1-GFP mice. En-face images for several retinal depths are displayed. By 1, 3 and 7 days post-lesion, microglia have migrated into the outer retina, many appearing amoeboid and displaying fewer laterally-branching projections. Despite the deep microglial response, neutrophils stay within the inner retina and are not found in the avascular outer retinal layers. Scale bar = 40 µm.

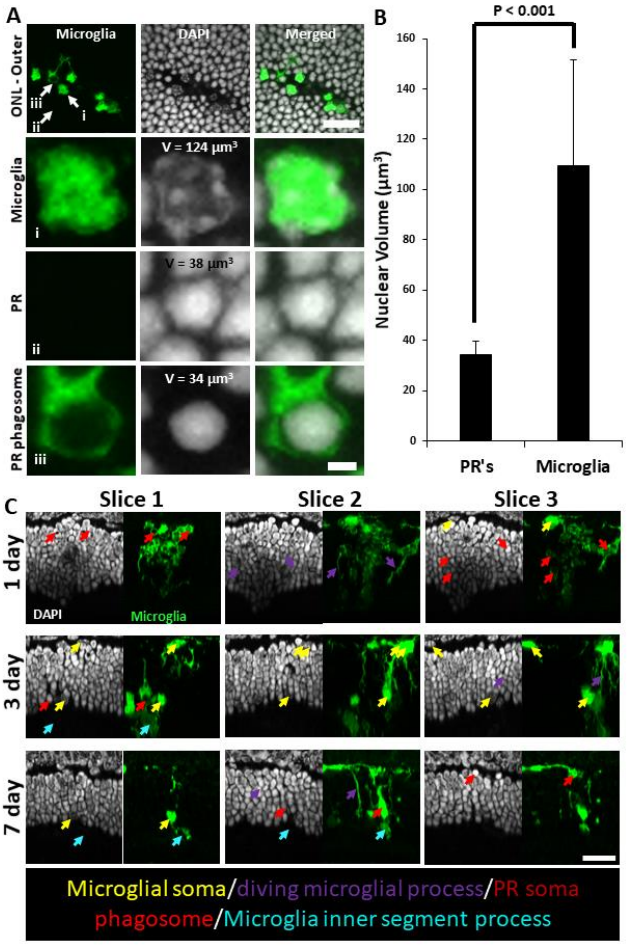

Figure 9 – figure supplement 2 Microglial PR phagosomes in the outer retina assessed with *ex vivo* confocal imaging. **(A)** En-face images of outer ONL in a DAPI-stained CX3CR1-GFP mouse 3 days post-laser-injury (top row). Microglia have infiltrated deep into the ONL and several PR phagosomes were identified. White arrows indicate locations for a single microglia (i), PR (ii) and PR phagosome (iii). These locations were expanded and displayed below. Microglia exhibited a heterogeneous nuclear staining pattern while PR nuclei exhibited homogenous DAPI fluorescence pattern. PR's displayed this pattern regardless of whether they were within a microglial phagosome or not. Top scale bar = 20 µm, bottom scale bar = 2 µm**. (B)** A finely-sliced (0.1 µm step size) outer retinal z-stack of DAPI-stained CX3CR1-GFP retina was used to quantify the average nuclear volume for infiltrated microglia (n = 14 nuclei) and PR's (n = 20 nuclei) for the same lesion site presented in A. On average, microglia had a statistically significant ($p < 0.001$) nuclear volume that was >3x that of PR's. These measurements allowed us to discriminate microglial somas from PR phagosomes. Error bars display mean + 1 SD. **(C)** Cross sections of DAPI-

stained outer retina in CX3CR1-GFP mice for 1, 3 and 7 days post-laser injury (n=3 mice). 3 representative planes (X-Z) through the lesion are displayed for each time point. Microglia form PR phagosomes within the ONL and microglial processes were seen extended into the PR inner/outer segment layer. Arrows label various morphological features seen at lesion sites: microglial somas (yellow), diving microglial process (violet), PR phagosome (red), microglial inner/outer segment process (cyan). Scale bar = 20 μm.

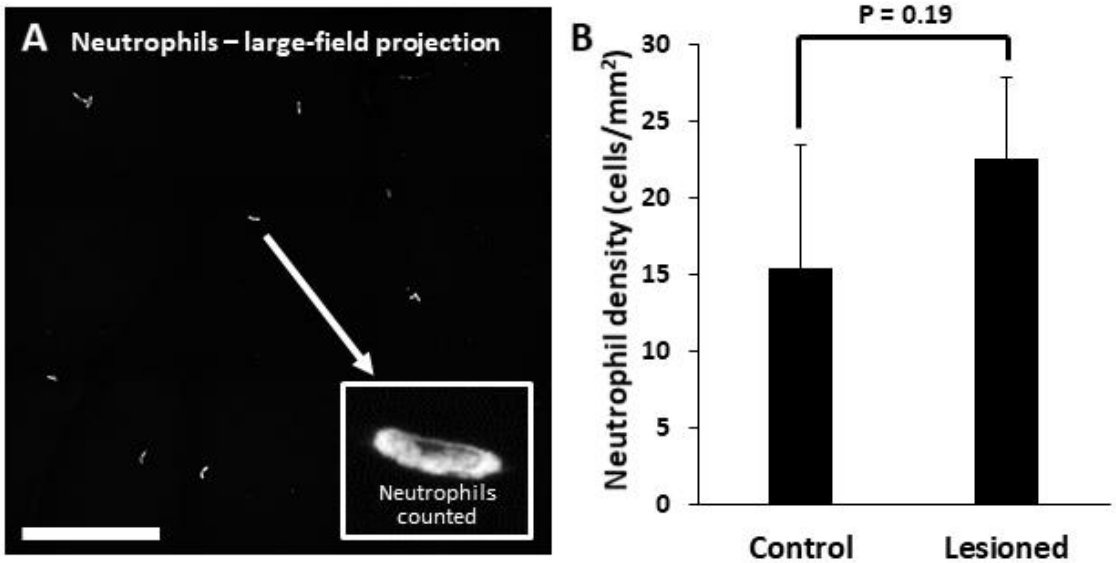

Figure 10. Quantification of neutrophils in laser damaged retinas assessed with ex vivo confocal microscopy over a wide-field. **(A)** Representative image displays neutrophils quantified using large-field (796 x 796 μm) z-stacks for control or 1 day after injury time points. In both control and laser injured retinas, neutrophils were sparse and confined to locations within capillaries suggesting they were the native fraction of circulating neutrophils at time of death. Inset displays expanded image of a single neutrophil. Scale bar = 200 μm. **(B)** Neutrophils quantified and displayed as the number of neutrophils per retinal area. The difference in number of neutrophils in control vs lesioned retinas was not statistically significant ($p = 0.19$). Error bars display mean + 1 SD.

Refer to .avi file

Video 1 Rotating 3D cubes of outer retinal nuclei and microglia after focal laser injury. Outer retinal Z-stacks of DAPI-stained whole-mount CX3CR1-GFP retinal tissue were imaged for control, 1, 3, 7 day and 2 month time points (n = 5 mice). DAPI + microglia composite cubes are displayed above and microglia cubes are displayed below. By 1 day, microglia send projections into the ONL, by 3 and 7 days, microglial somas have migrated into the ONL. Microglia within the ONL exhibit different morphology compared to the baseline condition. By 2 months, microglia are found back within the OPL, exhibiting lateral projections, similar to baseline. Scale bar = 40 μm.

Refer to .avi file

Video 2 Rotating 3D cubes of single neutrophils after laser injury or endotoxin induced uveitis. *Ex vivo* confocal z-stacks (0.1 μm steps) allowed detailed visualization of single neutrophils at 1 day after laser injury or 1 day after intravitreal LPS injection. After laser injury, neutrophils maintain a tubular, pill-shaped morphology (left). Occasionally, they would come to rest at capillary branch points (middle). In the EIU model, neutrophils extravasate into the retinal parenchyma and exhibit more spheroid morphology (right). We did not observe neutrophils to exhibit the extravasated morphology in response to laser injury.

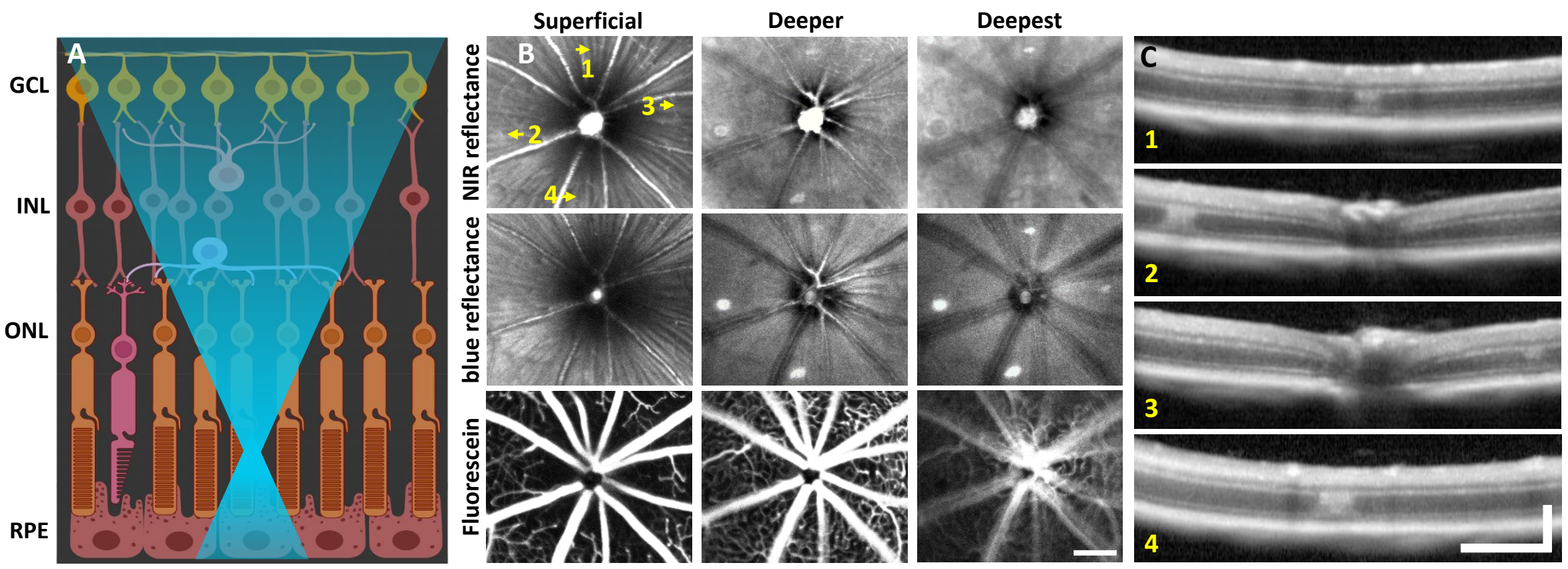
A
GCL
INL
ONL
RPE
Superficial
Deeper
Deepest
B
NIR reflectance
blue reflectance
Fluorescein
1
2
3
4
C
1
2
3
4

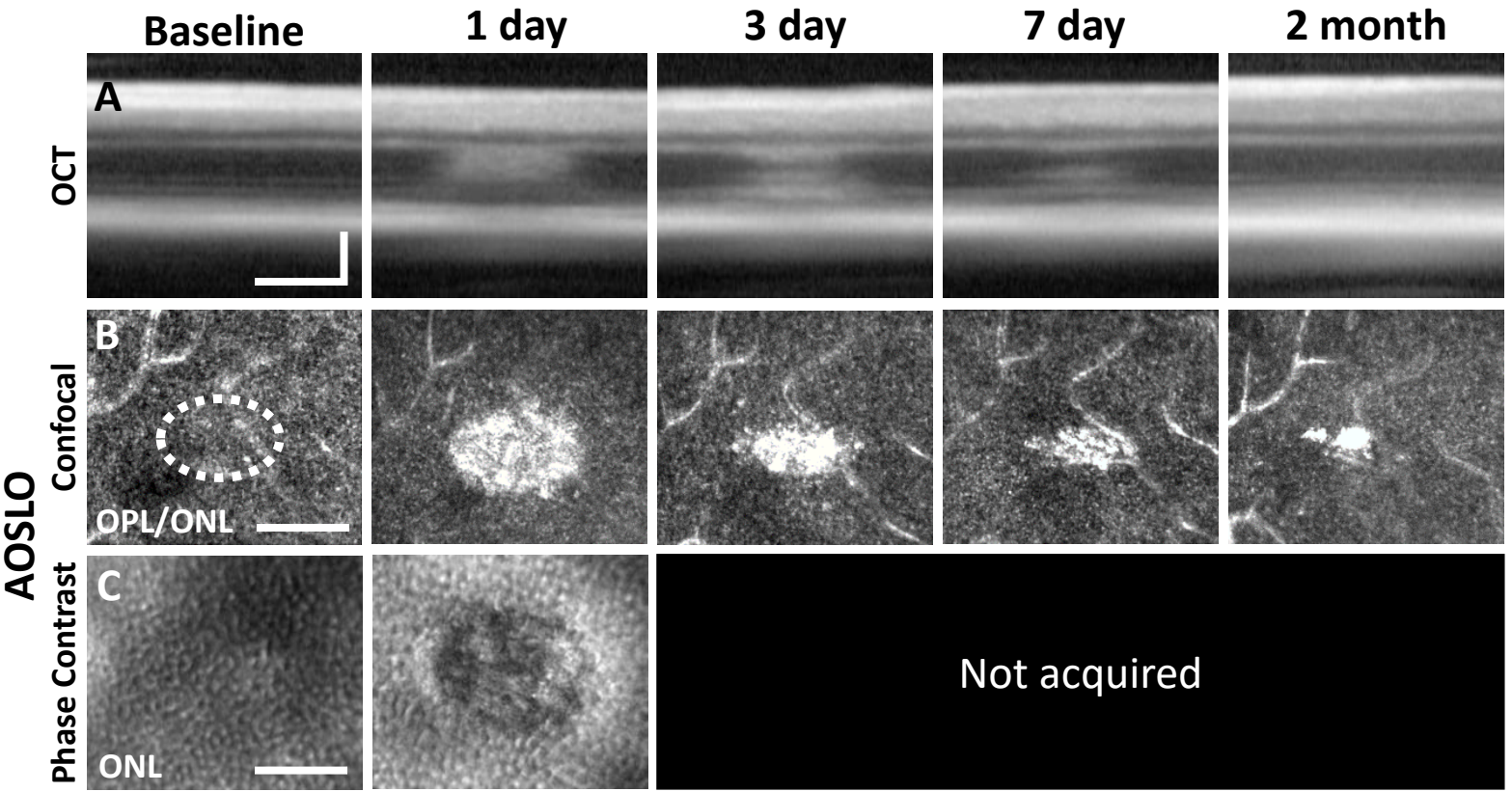
Baseline
1 day
3 day
7 day
2 month
A
OCT
B
Confocal
OPL/ONL
AOSLO
C
Phase Contrast
ONL
Not acquired

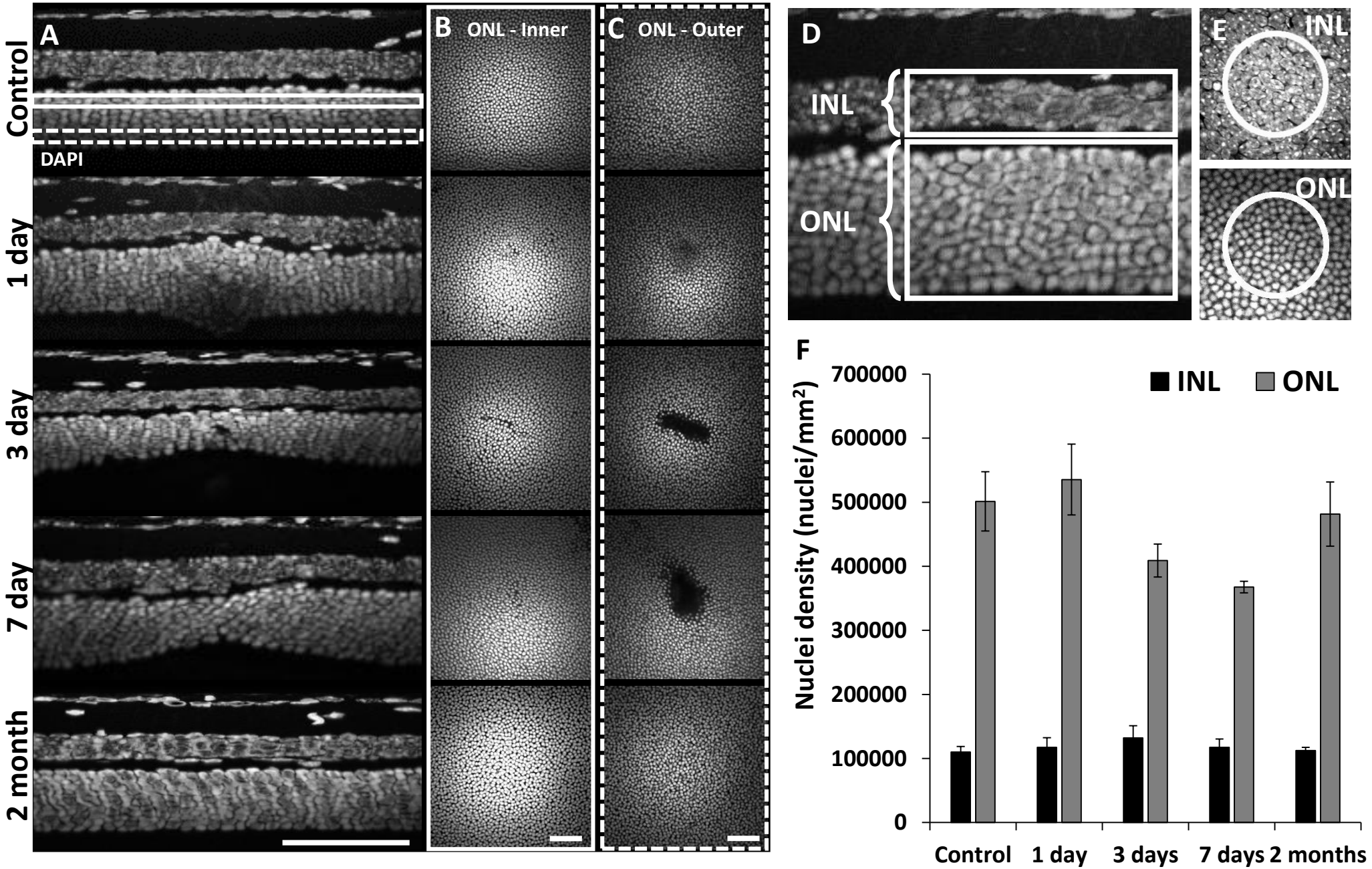
A
B ONL - Inner
C ONL - Outer
Control
DAPI
1 day
3 day
7 day
2 month
D
INL
ONL
E
INL
ONL
F
INL
ONL
Nuclei density (nuclei/mm²)
700000
600000
500000
400000
300000
200000
100000
0
Control
1 day
3 days
7 days
2 months

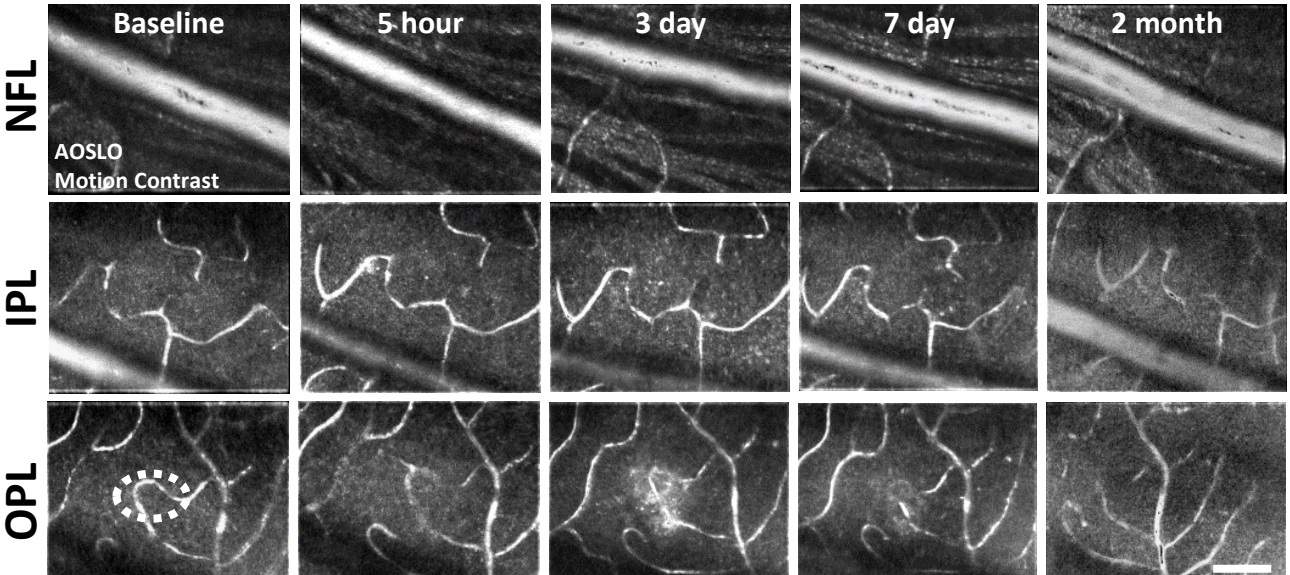
Baseline
5 hour
3 day
7 day
2 month
NFL
IPL
OPL
AOSLO
Motion Contrast

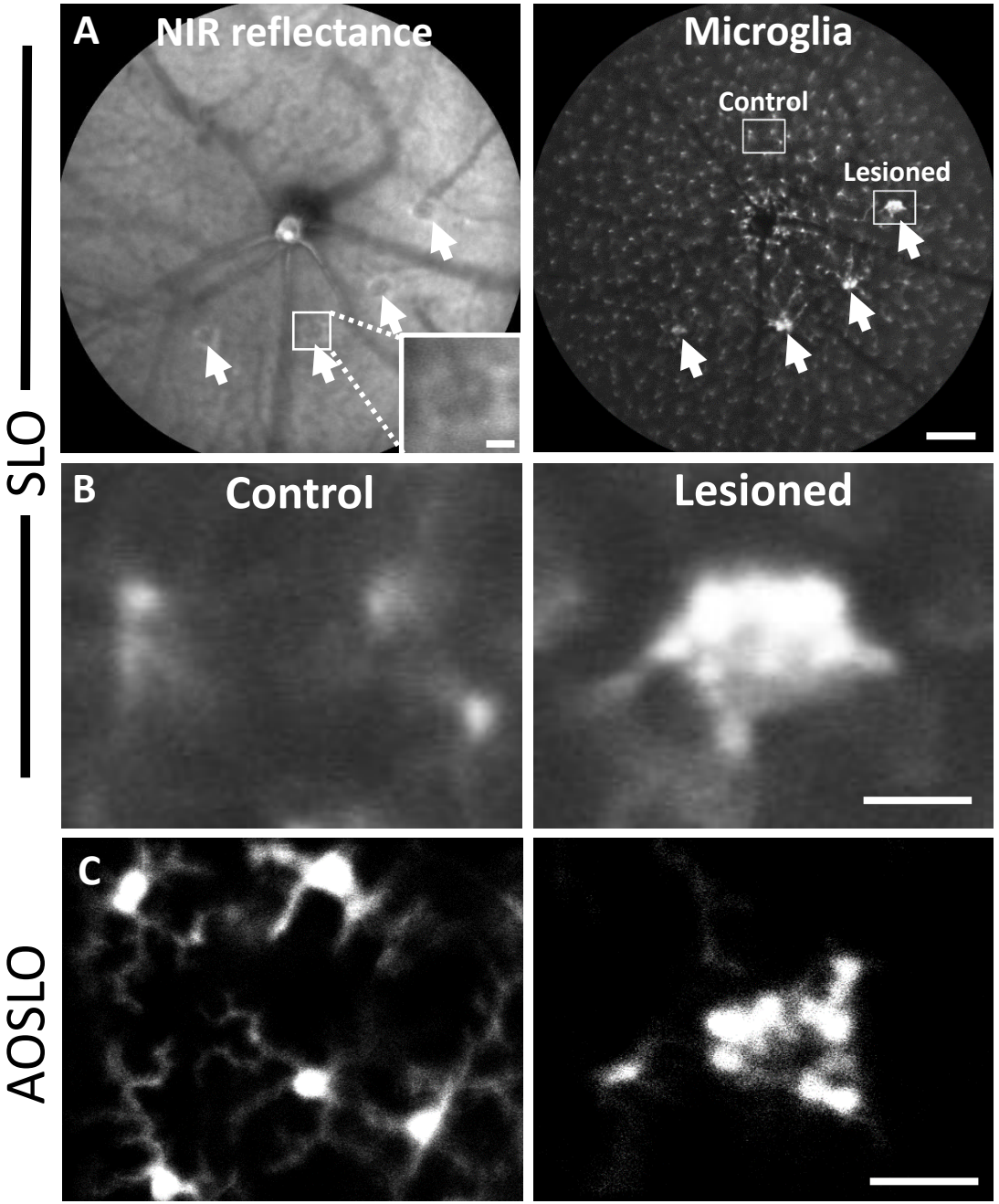
A
NIR reflectance
Microglia
Control
Lesioned
SLO
B
Control
Lesioned
C
AOSLO

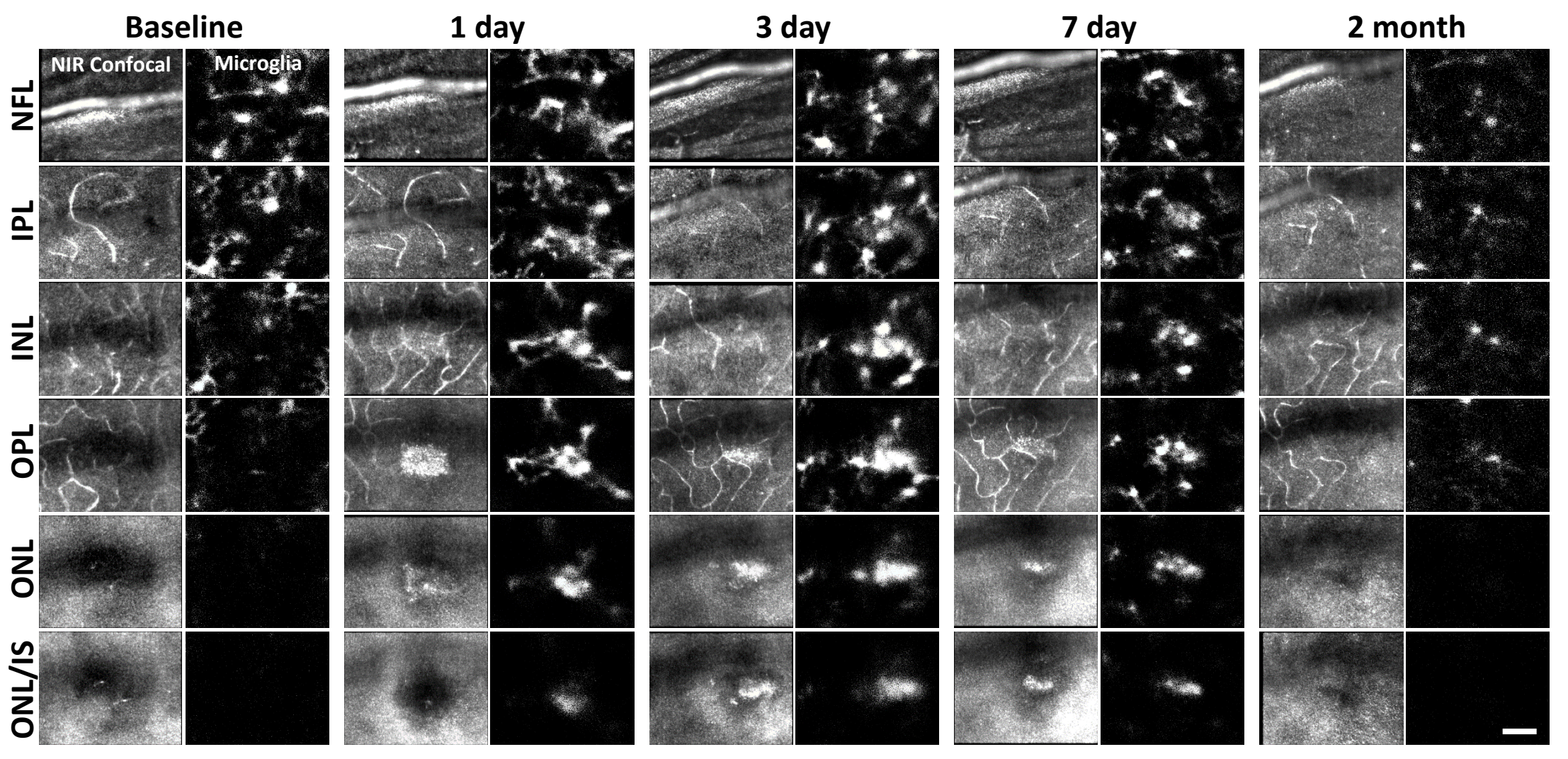
Baseline
1 day
3 day
7 day
2 month
NIR Confocal
Microglia
NFL
IPL
INL
OPL
ONL
ONL/IS

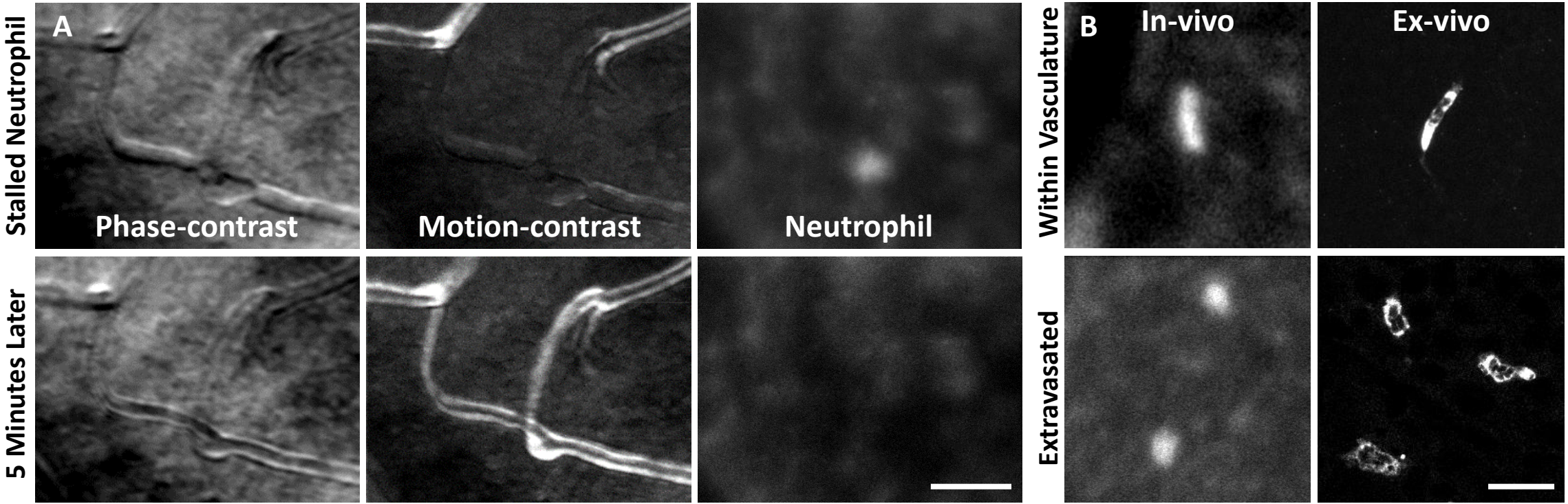
A
Stalled Neutrophil
5 Minutes Later
Phase-contrast
Motion-contrast
Neutrophil
B
Within Vasculature
Extravasated
In-vivo
Ex-vivo

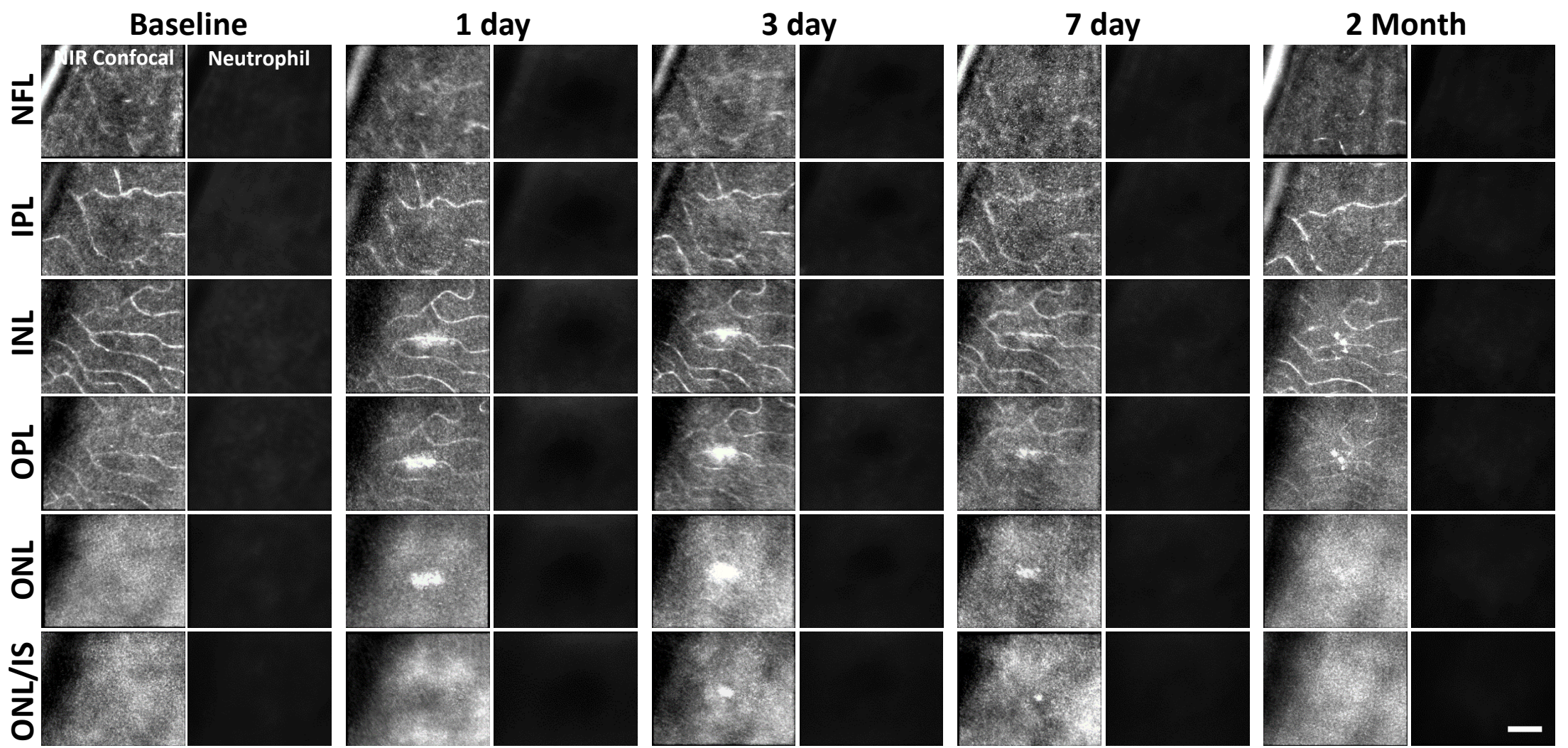
Baseline
1 day
3 day
7 day
2 Month
NIR Confocal
Neutrophil
NFL
IPL
INL
OPL
ONL
ONL/IS

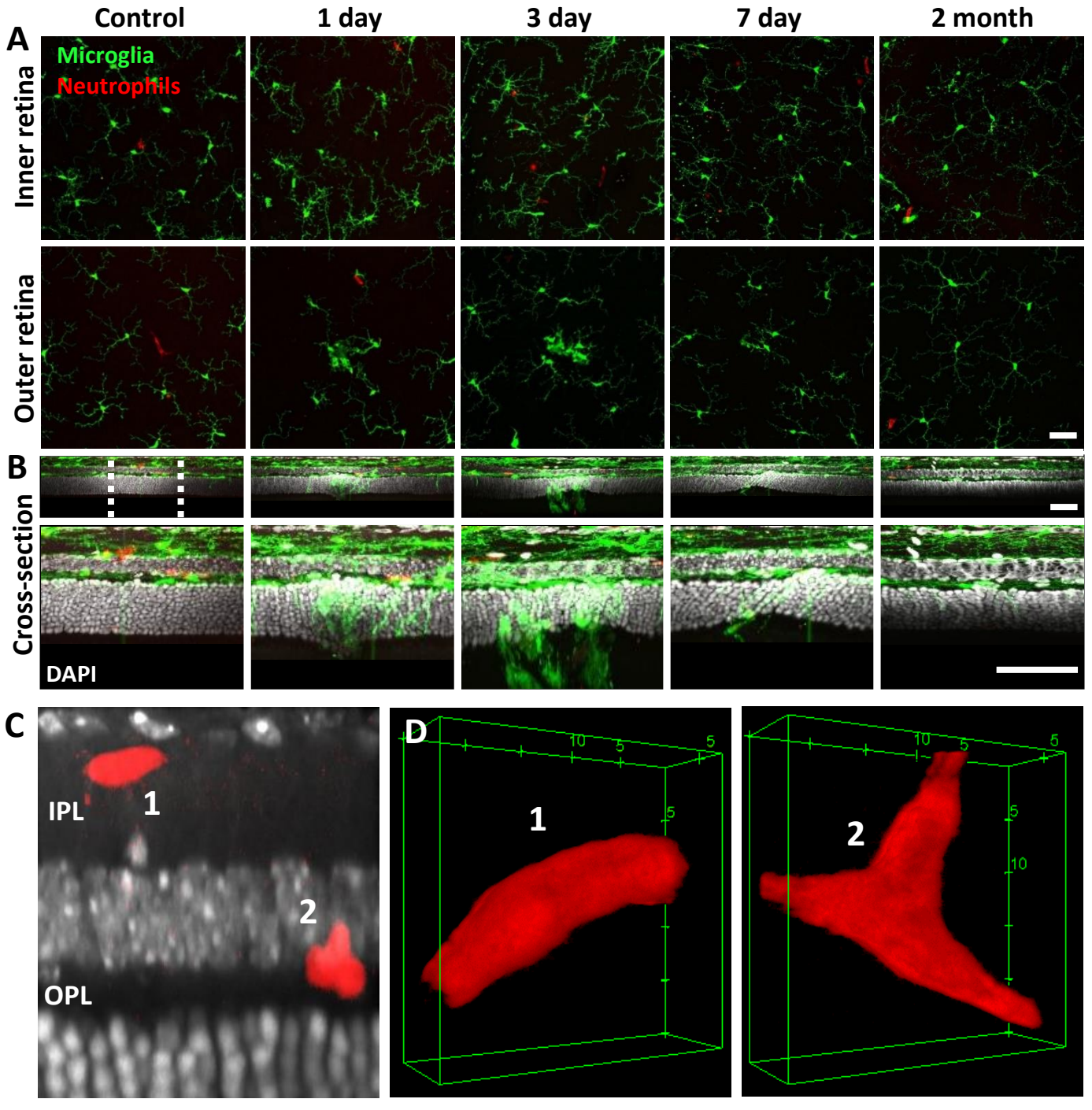
Control
1 day
3 day
7 day
2 month
A
Microglia
Neutrophils
Inner retina
Outer retina
B
Cross-section
DAPI
C
IPL
1
2
OPL
D
1
2

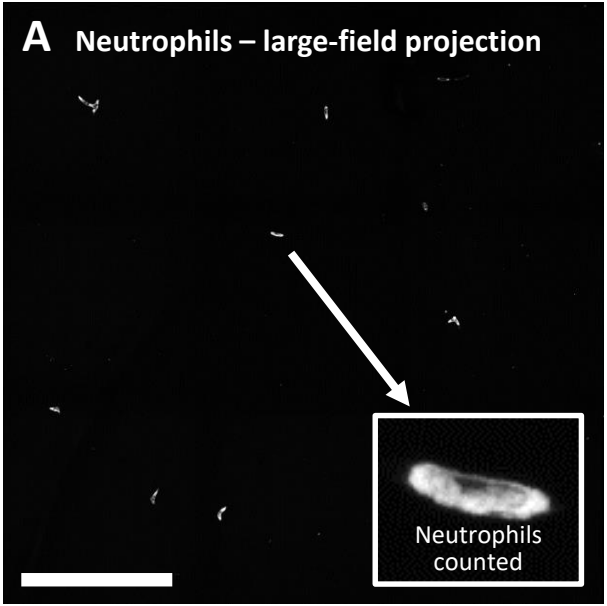
A
Neutrophils – large-field projection
Neutrophils counted

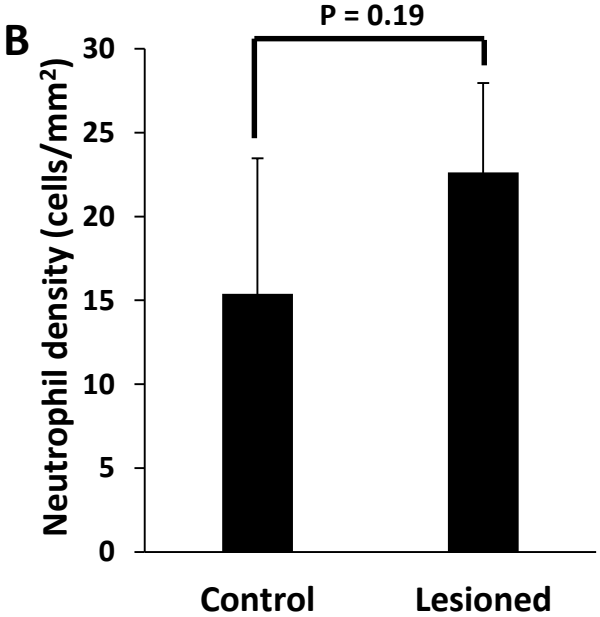
B
P = 0.19
Neutrophil density (cells/mm²)
30
25
20
15
10
5
0
Control
Lesioned

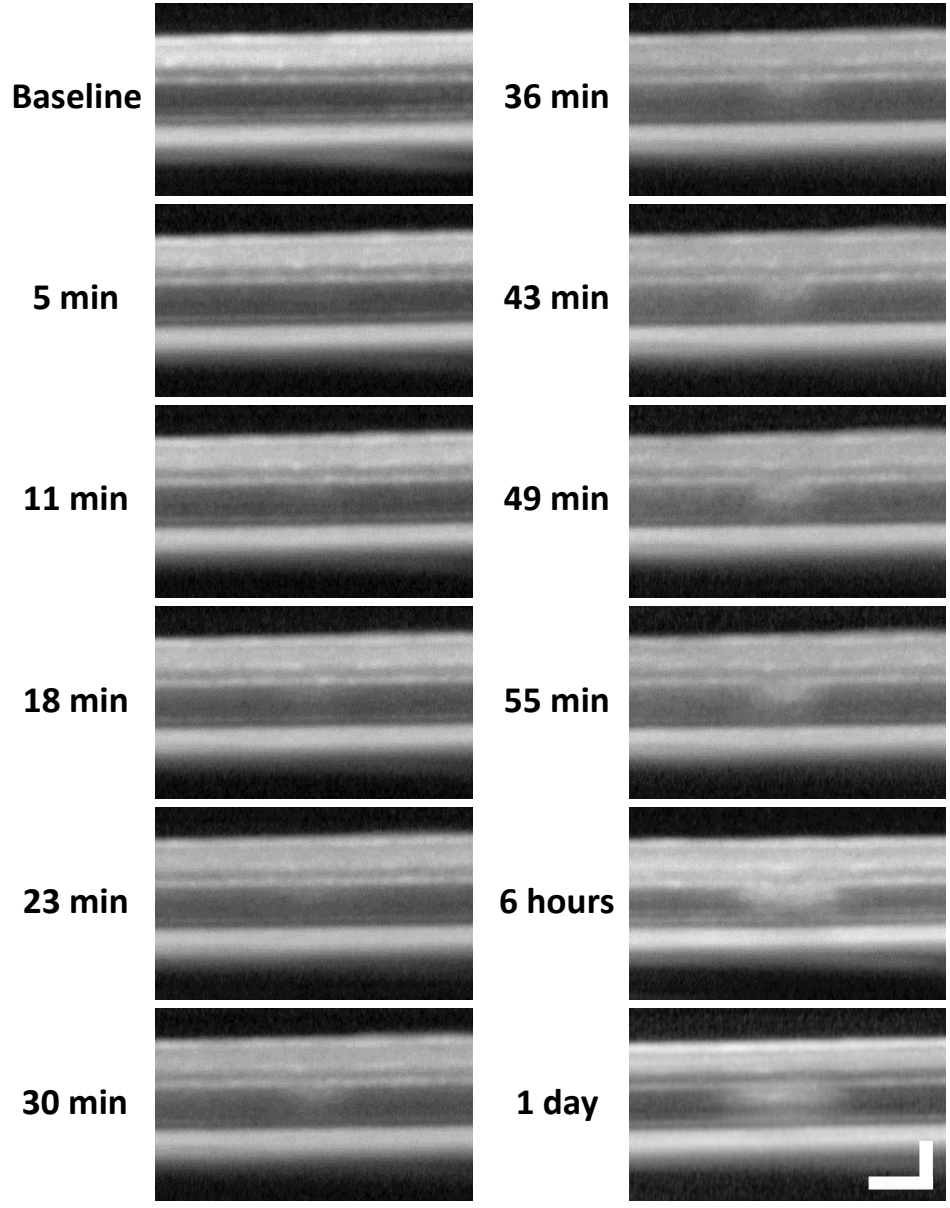
Baseline
5 min
11 min
18 min
23 min
30 min
36 min
43 min
49 min
55 min
6 hours
1 day

Mouse 1 – Flux measured for axially separate capillaries

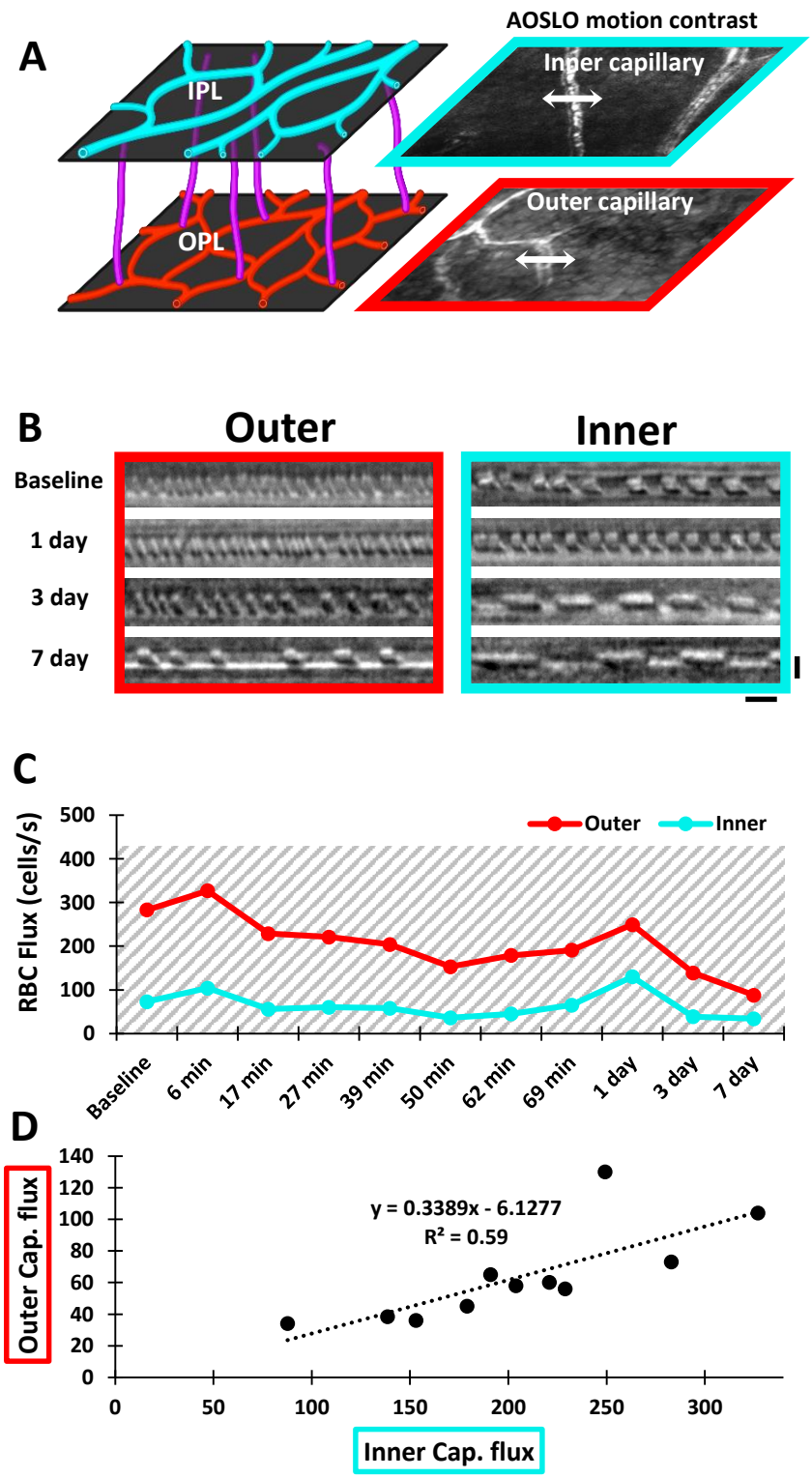

Mouse 2 – Flux measured for laterally separate capillaries

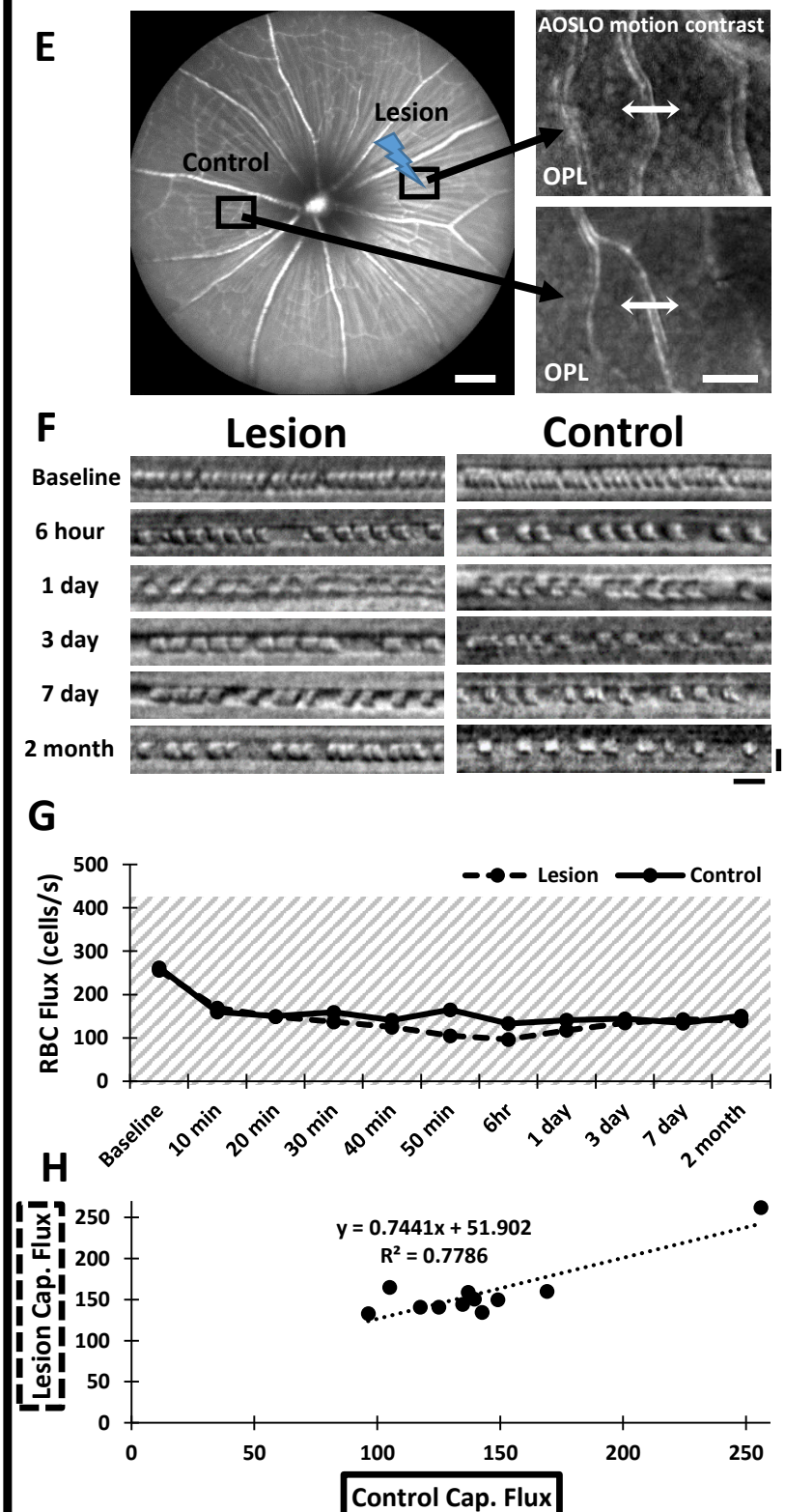

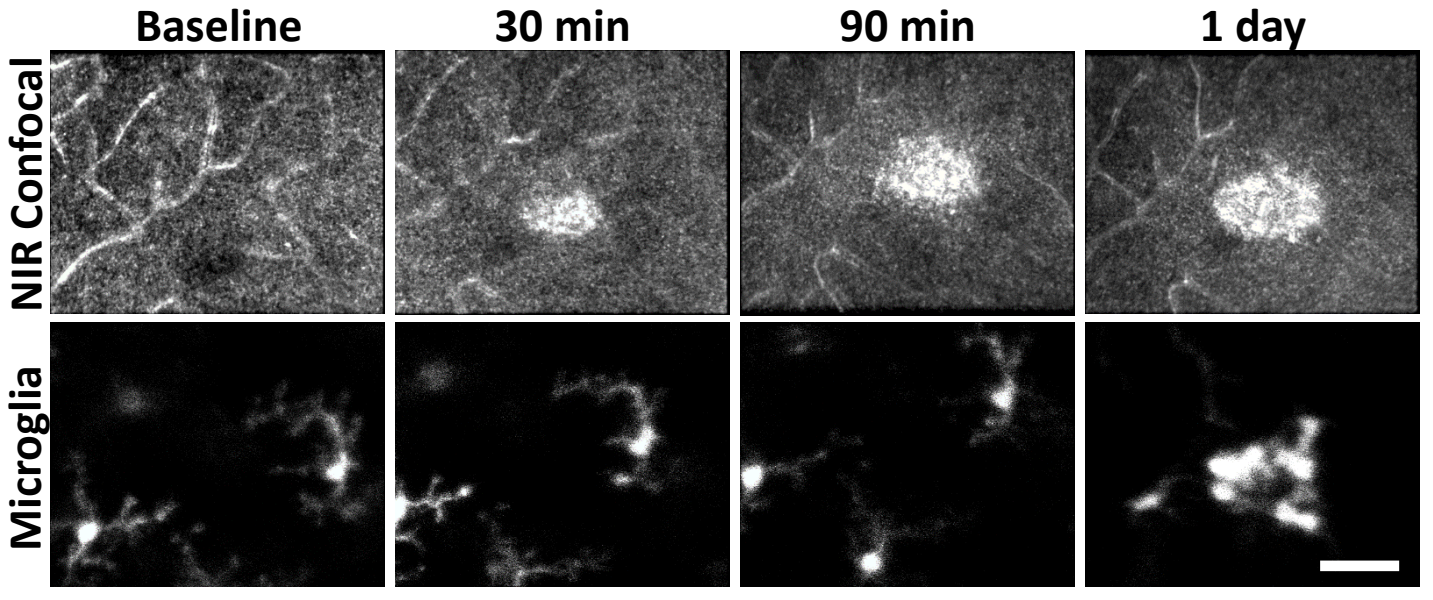
Baseline
30 min
90 min
1 day
NIR Confocal
Microglia

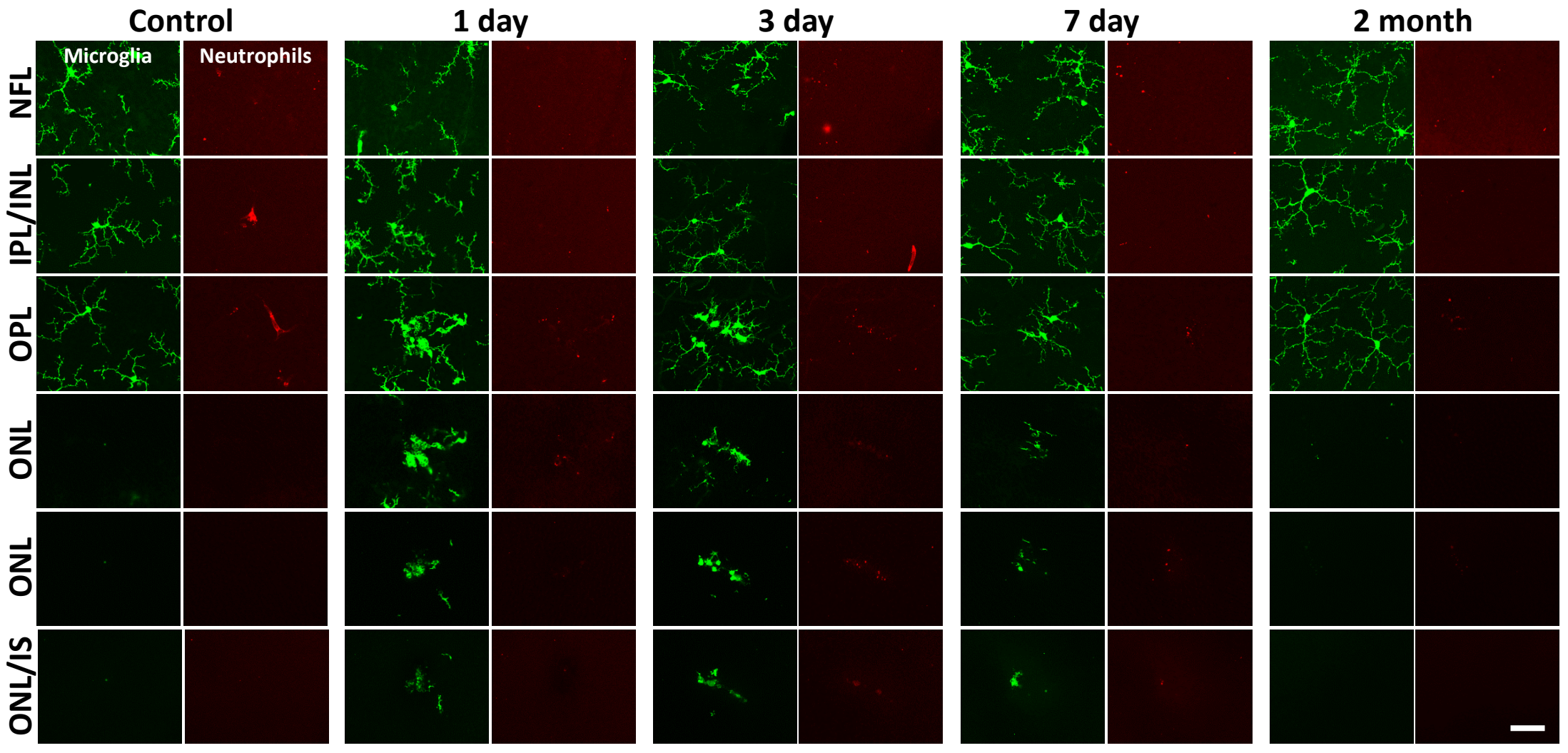
Control
1 day
3 day
7 day
2 month
Microglia
Neutrophils
NFL
IPL/INL
OPL
ONL
ONL
ONL/IS

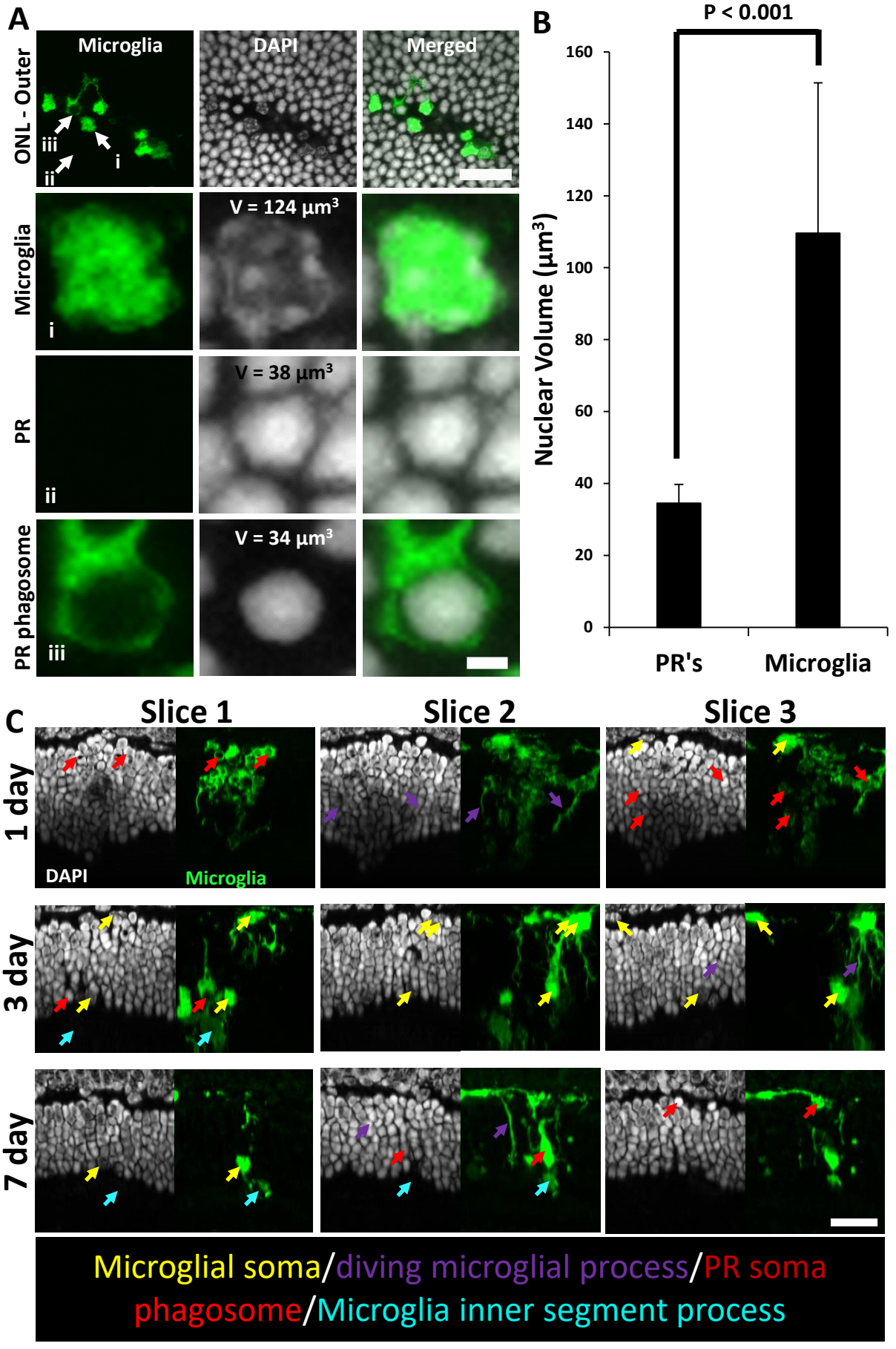
A
Microglia
DAPI
Merged
ONL - Outer
iii
i
ii
Microglia
V = 124 µm³
i
PR
V = 38 µm³
ii
PR phagosome
V = 34 µm³
iii
B
P < 0.001
Nuclear Volume (µm³)
160
140
120
100
80
60
40
20
0
PR's
Microglia
C
Slice 1
Slice 2
Slice 3
1 day
DAPI
Microglia
3 day
7 day
Microglial soma/diving microglial process/PR soma
phagosome/Microglia inner segment process